Overview of aerosol optical properties over southern West Africa from DACCIWA aircraft measurements

Cyrielle Denjean[1], Thierry Bourrianne[1], Frederic Burnet[1], Marc Mallet[1], Nicolas Maury[1], Aurélie Colomb[2], Pamela Dominutti[2,*], Joel Brito[2,**], Régis Dupuy[2], Karine Sellegri[2], Alfons Schwarzenboeck[2], Cyrille Flamant[3], Peter Knippertz[4]

[1]CNRM, Université de Toulouse, Météo-France, CNRS, Toulouse, France
[2]LaMP, Université de Clermont Auvergne, Clermont-Ferrand, France
[3]LATMOS/IPSL, Sorbonne Université, UVSQ, CNRS, Paris, France
[4]Institute of Meteorology and Climate Research, Karlsruhe Institute of Technology, Karlsruhe, Germany
* Now at Wolfson Atmospheric Chemistry Laboratories, Department of Chemistry, University of York, YO10 5DD- York, UK
** Now at: IMT Lille Douai, Université de Lille, SAGE, Lille, France

Correspondence to : Cyrielle Denjean (cyrielle.denjean@meteo.fr)

Abstract. Southern West Africa (SWA) is an African pollution hotspot but a relatively poorly sampled region of the world. We present an overview of *in-situ* aerosol optical measurements collected over SWA in June and July 2016 as part as the DACCIWA (Dynamics-Aerosol-Chemistry-Clouds Interactions in West Africa) airborne campaign. The aircraft sampled a wide range of air masses, including anthropogenic pollution plumes emitted from the coastal cities, long-range transported biomass burning plumes from Central and Southern Africa and dust plumes from the Sahara and Sahel region, as well as mixtures of these plumes. The specific objective of this work is to characterize the regional variability of the vertical distribution of aerosol particles and their spectral optical properties (single scattering albedo: *SSA*, asymmetry parameter, extinction mass efficiency, scattering Ångström exponent and absorption Ångström exponent: *AAE)*. First findings indicate that aerosol optical properties in the planetary boundary layer were dominated by a widespread and persistent biomass burning loading from the Southern Hemisphere. Despite a strong increase of aerosol number concentration in air masses downwind of urban conglomerations, spectral *SSA* were comparable to the background and showed signatures of the absorption characteristics of biomass burning aerosols. In the free troposphere, moderately to strongly absorbing aerosol layers, dominated by either dust or biomass burning particles, occurred

35   occasionally. In aerosol layers dominated by mineral dust particles, *SSA* varied from 0.81 to 0.92 at

36   550 nm depending on the variable proportion of anthropogenic pollution particles externally mixed

37   with the dust. For the layers dominated by biomass burning particles, aerosol particles were

38   significantly more light absorbing than those previously measured in other areas (e.g. Amazonia,

39   North America) with *SSA* ranging from 0.71 to 0.77 at 550 nm. The variability of *SSA* was mainly

40   controlled by variations in aerosol composition rather than in aerosol size distribution.

41   Correspondingly, values of *AAE* ranged from 0.9 to 1.1, suggesting that lens-coated black carbon

42   particles were the dominant absorber in the visible range for these biomass burning aerosols.

43   Comparison with literature shows a consistent picture of increasing absorption enhancement of

44   biomass burning aerosol from emission to remote location and underscores that the evolution of

45   *SSA* occurred a long time after emission.

46   The results presented here build a fundamental basis of knowledge about the aerosol optical

47   properties observed over SWA during the monsoon season and can be used in climate modelling

48   studies and satellite retrievals. In particular and regarding the very high absorbing properties of

49   biomass burning aerosols over SWA, our findings suggest that considering the effect of internal

50   mixing on absorption properties of black carbon particles in climate models should help better

51   assessing the direct and semi-direct radiative effects of biomass burning particles.

52

1. Introduction

54   Atmospheric aerosols play a crucial role in the climate system by altering the radiation budget

55   through scattering and absorption of solar radiation and by modifying cloud properties and

56   lifetime. Yet considerable uncertainties remain about the contribution of both natural and

57   anthropogenic aerosol to the overall radiative effect *(Boucher et al., 2013)*. Large uncertainties are

58   related to the complex and variable properties of aerosol particles that depend on the aerosol

59   source and nature as well as on spatial and temporal variations. During transport in the

60   atmosphere, aerosol particles may undergo physical and chemical aging processes altering the

61   composition and size distribution and henceforth the optical properties and radiative effects. The

62   capability of reproducing this variability in climate models represents a real challenge *(Myhre et*

63   *al., 2013; Stier et al., 2013; Mann et al., 2014).* Therefore, intensive experimental observations in

64   both aerosol source and remote areas are of paramount importance for constraining and evaluating

65   climate models.

66

67   Key parameters from a climate perspective are the aerosol vertical distribution and respective

68   spectral optical properties. Radiative transfer codes commonly incorporated in climate models and

69   in satellite data retrieval algorithms use single scattering albedo (*SSA)*, extinction mass efficiency

70   (*MEE)* and asymmetry factor (*g*) as input parameters. These parameters depend on the aerosol size

71   distribution, the real and imaginary parts of the refractive index (*m-ik*), and the wavelength of

72   incident light, λ. The knowledge of the vertical distribution of these fundamental parameters is

73   crucial to accurately estimate the direct and semi-direct radiative effects of aerosols as well as the

74   vertical structure of atmospheric heating rates resulting from absorption by particles. Above

75   information is also required to retrieve aerosol properties (aerosol optical depth, size distribution)

76   from remote sensing data.

77

78   Southern West Africa (SWA) is one of the most climate-vulnerable region in the world , where the

79   surface temperature is expected to increase by ~3°K at the end of the century (2071-2100) in the

80   Coupled Model Intercomparison Project Phase 5 (CMIP5) *(Roehrig et al., 2013)*. It is

81   characterized by a fast-growing population, industrialization and urbanization *(Liousse et al.,*

82   *2014)*. This is particularly the case along the Guinea Coast where several already large cities are

83   experiencing rapid growth *(Knippertz et al., 2015a)*. Despite these dramatic changes, poor

84   regulation strategies of traffic, industrial and domestic emissions lead to a marked increase of

85   anthropogenic aerosol loading from multiple sources including road traffic, industrial activities,

86   waste burning, ship plumes, domestic fires, power plants, etc. Tangible evidence for regional

87   transport of anthropogenic pollutants associated with urban emissions has altered air pollution

88   from a local issue to a regional issue and beyond *(Deetz et al., 2018; Deroubaix et al. 2019)*. This

89   is particularly the case during summer when land-sea breeze systems can develop and promote the

90   transport of pollutants inland, away from the urbanized coastal strip of SWA *(Flamant et al.,*

91   *2018a)*. In addition to this anthropogenic regional pollution, SWA is impacted by a significant

92   import of aerosols from remote sources. Biomass burning mainly from vegetation fires in Central

93   Africa are advected to SWA in the marine boundary layer and aloft *(Mari et al., 2008; Menut et al.*

94   *2018; Haslett et al., 2019)*. The nearby Sahara desert and the Sahel are large sources of natural

95   wind-blown mineral dust aerosol throughout the year with a peak in springtime *(Marticorena and*

96   *Bergametti, 1996)*. Biomass burning, dust and anthropogenic pollution aerosols can be mixed

97   along their transport pathways *(Flamant et al., 2018a; Deroubaix et al. 2019)*, resulting in

98   complex interactions between physical and chemical processes and even meteorological

99   feedbacks.

100

101   In West Africa, most of the aerosol–radiation interaction studies focused on optical properties of

102   dust and biomass burning aerosols in remote regions far from major sources of anthropogenic

pollution aerosol. They include ground-based and airborne field campaigns such as DABEX (Dust and Biomass Experiment, *Haywood et al., 2008)*, AMMA (Analysis Multidisciplinary of African Monsoon, *Lebel et al., 2010)*, DODO (Dust Outflow and Deposition to the Ocean, *McConnell et al., 2008)*, SAMUM-1 and SAMUM-2 (Saharan Mineral Dust Experiment, *Heintzenberg, 2009; Ansmann et al., 2011)* and AER-D (AERosol Properties – Dust, *Ryder al. 2018)*. These projects concluded that the influence of both mineral dust and biomass burning aerosols on the radiation budget is significant over West Africa, implying that meteorological forecast and regional/global climate models should include their different radiative effects for accurate forecasts and climate simulations. Over the Sahel region, *Solmon et al. (2008)* have highlighted the high sensitivity of mineral dust optical properties to precipitation changes at a climatic scale. However, the optical properties of aerosols particles in the complex chemical environment of SWA are barely studied. This is partly due to the historically low level of industrial developments of the region. Motivated by the quickly growing cities along the Guinea Coast, the study of transport, mixing, and feedback processes of aerosol particles is therefore very important for better quantification of aerosol radiative impact at the regional scale and improvement of climate and numerical weather prediction models.

In this context, the DACCIWA (Dynamics-Aerosol-Chemistry-Clouds Interactions in West Africa, *Knippertz et al., 2015b*) campaign, designed to characterize both natural and anthropogenic emissions over SWA, provides important and unique observations of aerosols in a region much more affected by anthropogenic emissions than previously thought. A comprehensive field campaign took place in June–July 2016 including extensive ground-based *(Kalthoff et al., 2018)* and airborne measurements *(Flamant et al., 2018b)*. In this study, we present an overview of *in-situ* airborne measurements of the vertical distribution of aerosol particles and their spectral optical properties acquired with the ATR-42 French research aircraft over the Guinea Coast.

Section 2 presents the flight patterns, instrumentation and data analysis. Section 3 provides an overview of the aerosol microphysical and optical properties. The impact of aging and mixing processes on aerosol optical properties is discussed in section 4 before conclusions are presented in section 5.

2. Methodology

2.1. ATR-42 measurements overview

This analysis focuses on flight missions conducted by the ATR-42 aircraft of SAFIRE (Service des Avions Français Instrumentés pour la Recherche en Environnement - the French aircraft service for environmental research) over the Gulf of Guinea and inland. A full description of flight patterns during DACCIWA is given in *Flamant et al. (2018b)*. Here we present results from 15 flights focused on the characterization of anthropogenic pollution, dust and biomass burning plumes. The flight tracks are shown in Figure 1 and a summary of flight information is provided in Appendix 1. The sampling strategy generally consisted of two parts: first, vertical soundings were performed from 60 m up to 8 km above mean sea level (amsl) to observe and identify interesting aerosol layers. Subsequently, the identified aerosol layers were probed with the *in-situ* instruments by straight levelled runs (SLR) at fixed flight altitudes.
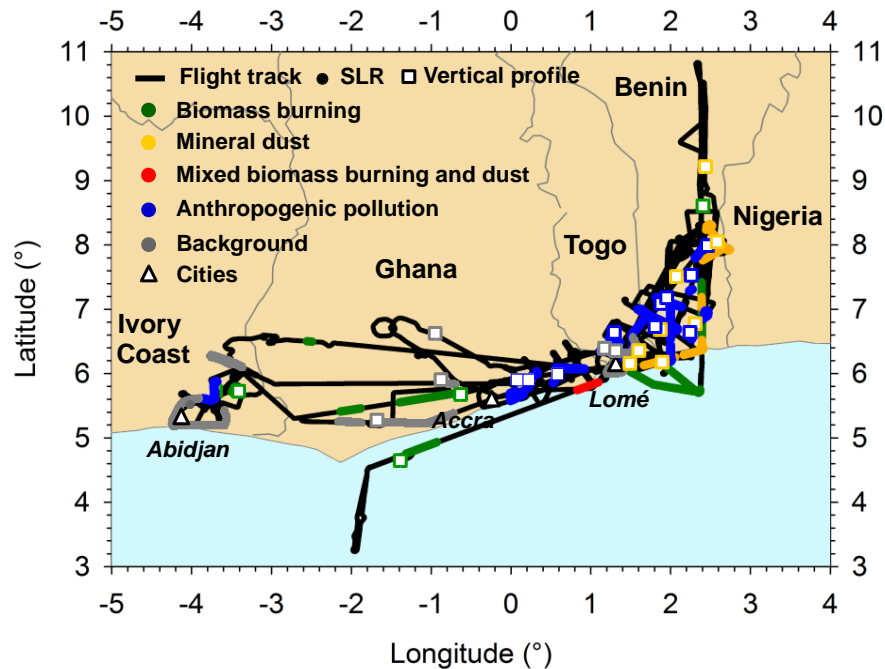
Figure 1. Tracks of the 15 flights analyzed in this study. The colors indicate aircraft flight sampling layers dominated by biomass burning (green), mineral dust (orange), mixed dust-biomass burning (red), anthropogenic pollution (blue) and background particles (grey) from both vertical profiles (squares) and straight and level runs (SLRs; dots).

The ATR-42 aircraft was equipped with a wide variety of instrumentation performing gas and aerosol measurements. The measured meteorological parameters include temperature, dew point temperature, pressure, turbulence, relative humidity, as well as wind speed and direction. Gas phase species were sampled through a rear facing ¼ inch Teflon tube. Carbon monoxide (CO) was

measured using ultra-violet and infrared analysers (PICARRO). The nitric oxide (NO) and nitrogen dioxide (NO_2) measurements were performed using an ozone chemiluminescence instrument (Thermo Environmental Instrument TEi42C with a Blue Light Converter for the NO2 conversion). On-board aerosol instruments sampled ambient air via stainless steel tubing through the Community Aerosol Inlet (CAI). This is an isokinetic and isoaxial inlet with a 50 % sampling efficiency for particles with a diameter of 5 μm *(Denjean et al., 2016).*

The total number concentration of particles larger than 10 nm (*Ntot*) was measured by a condensation particle counter (CPC model MARIE built by University of Mainz; *Mertes, Schröder, and Wiedensohler, 1995; Russell et al., 1996; Wiedensohler et al., 1997*). The aerosol size distribution was measured using an ultra-high sensitivity aerosol spectrometer (UHSAS, DMT), a custom-built scanning mobility sizer spectrometer (SMPS) and an optical particle counter (OPC, GRIMM model 1.109). Instrument calibration was performed with PSL nanospheres and oil particles size-selected by a differential mobility analyser (DMA) for diameters from 90 nm to 20 μm. The SMPS data acquisition system failed after two-third of the campaign and could not be repaired. We found the UHSAS to show false counts in the diameters below 100 nm. Therefore, these channels were disregarded in the data analysis.

The particle extinction coefficient (σ_{ext}) at the wavelength of 530 nm was measured with a cavity attenuated phase shift particle light extinction monitor (CAPS-PMex, Aerodyne Research). The particle scattering coefficients (σ_{scat}) at 450, 550 and 635 nm were measured using a TSI 3-wavelength nephelometer and corrected for angular truncator error in the data inversion procedure using a Mie code (i.e. Section 2.3.1 and Appendix 2). The absorption coefficients (σ_{abs}) at 467, 520 and 660 nm were measured by a Radiance Research Particle Soot Absorption Photometer (PSAP). The PSAP measures changes of filter attenuation due to the collection of aerosol deposited on the filter, which were corrected for the scattering artifacts according to the *Virkkula (2010)* method. Prior to the campaign, the CAPS was evaluated against the combination of the nephelometer and the PSAP. An instrument intercomparison was performed with purely scattering ammonium sulfate particles and with strongly absorbing black carbon particles (BC). Both types of aerosol were generated by nebulizing a solution of the respective substances and size-selected using a DMA. For instrument intercomparison purposes, σ_{ext} from the combination of nephelometer and PSAP was adjusted to that for 530 nm by using the scattering and absorption Ångstrom exponent (*SAE* and *AAE*, respectively). The instrument evaluation showed an excellent accuracy of the CAPS measurements by comparison to the nephelometer and PSAP combination.

2.2. Ancillary products

In order to determine the history of air masses prior aircraft sampling, backward trajectories and satellite images were used. The trajectories were computed using the Hybrid Single Particle Lagrangian Integrated Trajectory Model (HYSPLIT) and the National Centers for Environmental Prediction (NCEP) Global Data Assimilation System (GDAS) data with 0.5° horizontal resolution for sequences and times of interest. We compared the backward trajectory heights with information of fire burning times (e.g. MODIS Burnt Area Product) and dust release periods (e.g. Meteosat Second Generation (MSG) dust RGB composite images) to assess the aerosol source regions of the investigated air masses. The air masses represented by the trajectory are assumed to obtain their aerosol loading from source regions when the trajectory passes over regions with significant dust activation and/or fire activity at an altitude close to the surface. Trajectory calculations with slightly modified initial conditions with respect to the arrival time, location and altitude were performed to check the reliability of the location of source regions. Uncertainties in this approach, caused by unresolved vertical mixing processes, and by general uncertainties of the trajectory calculations are estimated to be in the range of 15–20 % of the trajectory distance *(Stohl et al., 2002)*.

2.3. Data analysis

In the following, extensive aerosol parameters (concentrations, scattering, absorption and extinction coefficients) are converted to standard temperature and pressure (STP) using T = 273 K and P = 1013.25 hPa. The STP concentration data correspond to mixing ratios, which are independent of ambient pressure and temperature during the measurement. In the analysis, the data were averaged over sections of SLR with homogeneous aerosol conditions outside of clouds.

2.3.1. Derivation of aerosol microphysical and optical properties

Appendix 2 and Table 1 show the iterative procedure and the equations used to calculate the aerosol microphysical and optical parameters as briefly explained below.

The particle number concentration in the coarse mode (N_{coarse}) was calculated by integrating the OPC size distributions over the range 1 to 5 μm. The signal to noise ratio of the OPC for particles in this size range was higher than 3, which makes the instrument well suited to quantify variations in N_{coarse}. The number concentration of particles in the fine mode (N_{fine}) was obtained as the difference between total number concentration (N_{tot} particle diameter range above 5 nm) measured by the CPC and N_{coarse}.

224

225 For optical calculations, the 3λ-σ_{abs} from the PSAP were adjusted at the 3 wavelengths measured

226 by the nephelometer using the *AAE* calculated from the 3λ measured σ_{abs}. Once σ_{scat} and σ_{abs}

227 obtained at the same wavelength, an optical closure study estimated the complex refractive index

228 based on optical and size data. Optical calculations were performed using Mie theory, implying a

229 sphericity assumption, because it facilitates a quantitative comparison with past data, mostly using

230 this simplification and because most climate models assume spherical properties. The retrieval

231 algorithm consists of iteratively varying the real part of the complex refractive index *(m)* from 1.33

232 to 1.60 and the imaginary part of the complex refractive index *(k)* from 0.000 to 0.080 in steps of

233 resolution of 0.001. *m* and *k* were fixed when the difference between calculated values of σ_{scat} and

234 σ_{abs} and measurements was below 1%. Given that the size distribution measured by the UHSAS

235 and the OPC depends on *n*, the optical-to-geometrical diameter conversion was recalculated at

236 each iteration based on the assumed *n*. The resulting number size distributions from SMPS,

237 UHSAS and OPC were parameterized by fitting four log-normal distributions and used as input

238 values in the optical calculations. Once *n* and *k* were obtained at 3λ, we estimated the following

239 optical parameters:

240 - *SAE* depends on the size of the particles. Generally, it is lower than 0 for aerosols dominated by

241 coarse particles, such as dust aerosols, but it is higher than 0 for fine particles, such as

242 anthropogenic pollution or biomass burning aerosol *(Seinfeld and Pandis, 2006; Schuster et al.,*

243 *2006)*.

244 - *AAE* provides information about the chemical composition of atmospheric aerosols. BC absorbs

245 radiation across the whole solar spectrum with the same efficiency, thus it is characterized by *AAE*

246 values around 1. Conversely, mineral dust particles show strong light absorption in the blue to

247 ultraviolet spectrum leading to *AAE* values up to 3 *(Kirchstetter et al., 2004; Petzold et al., 2009)*.

248 - *SSA* describes the relative importance of scattering and absorption for radiation. Thus, it indicates

249 the potential of aerosols for cooling or warming the lower troposphere.

250 - *g* describes the probability of radiation to be scattered in a given direction. Values of *g* can range

251 from −1 for entirely backscattered light to +1 for complete forward scattering light.

252 - *MEE* represents the total light extinction per unit mass concentration of aerosol. The estimates of

253 *MEE* assume mass densities of 2.65 g cm^3 for dust aerosol, 1.35 g cm^3 for biomass burning

254 aerosol, 1.7 g cm^3 for anthropogenic aerosol and 1.49 g cm^3 for background aerosol *(Hess et al.,*

255 *1998; Haywood et al., 2003a)*.

Aerosol parameters	Symbol	λ (nm)	Method
Aerosol microphysical properties			
Total number concentration	N_{tot}	-	Measured by a CPC in the particle diameter range above 5 nm
Number concentration in the coarse mode	N_{coarse}	-	GRIMM size distributions integrated on the range 1 to 5 μm.
Number concentration in the fine mode	N_{fine}	-	Difference N_{tot} and N_{coarse}.
Number size distribution	dN/dlogDp	-	$dN/dlogDp = \Sigma_{i=1}^{4} (N_{tot,i}\ exp(-(logD_p - logD_{p,g,i})^2/(2\ log\ \sigma_i))/(\sqrt{2}\ log\ \sigma_i))$ with $N_{tot,i}$ the integrated number concentration, $D_{p,g,i}$ the geometric median diameter and σ_i geometric standard deviation for each mode i
Volume size distribution	dV/dlogDp	-	$dV/dlogDp = \Sigma_{i=1}^{4} (N_{tot,i}\ D_p^3\ \pi/6\ exp(-(logD_p - logD_{p,g,i})^2/(2\ log\ \sigma_i))/(\sqrt{2}\ log\ \sigma_i))$
Aerosol optical properties			
Scattering coefficient	σ_{scat}	450, 550, 635	Measured by the nephelometer and corrected for truncator error
Absorption coefficient	σ_{abs}	467, 520, 660	Measured by the PSAP and corrected for filter based artefacts
Extinction coefficient	σ_{ext}	530	Measured by the CAPS
Scattering Ångström exponent	*SAE*	450 to 700	Calculated from the nephelometer measurements : $SAE = -ln\ (\sigma_{scat}(450)/\sigma_{scat}(700))\ /\ ln\ (450/700)$
Absorption Ångström exponent	*AAE*	440 to 660	Calculated from the PSAP measurements : $AAE = -ln(\sigma_{abs}(467)/\sigma_{abs}(660))\ /\ ln\ (467/660)$
Complex refractive index	*n*	450, 550, 660	Inversion closure study using Mie theory (Fig. A2) $n(\lambda) = m(\lambda)-ik(\lambda)$
Single scattering albedo	*SSA*	450, 550, 660	Inversion closure study using Mie theory (Fig. A2) $SSA(\lambda) = \sigma_{scat}(\lambda)/\sigma_{ext}(\lambda)$
Mass extinction efficiency	*MEE*	450, 550, 660	Inversion closure study using Mie theory (Fig. A2) $MEE(\lambda) = \sigma_{ext}(\lambda)/C_m$ with C_m the aerosol mass concentration
Asymmetry parameter	*g*	450, 550, 660	Inversion closure study using Mie theory (Fig. A2) $g(\lambda) = 1/2\ \int_0^\pi cos(\Theta)sin(\Theta)P(\Theta,\lambda)d(\Theta)$ with $P(\Theta,\lambda)$ the scattering phase function and Θ the scattering angle.

257   **Table 1. Aerosol microphysical and optical properties derived in this work**

258

2.3.2. Classification of aerosols plumes

Data were screened in order to isolate plumes dominated by anthropogenic pollution from urban emissions, biomass burning and mineral dust particles, resulting in a total number of 19, 12 and 8 genuine plume interceptions, respectively, across the 15 flights. As shown in Figure 2, identification of the plumes was based on a combination of CO and NOx (sum of NO and NO_2) concentrations, as well as *AAE* and *SAE* that have been shown to be good parameters for classifying aerosol types *(Kirchstetter et al., 2004; Petzold et al., 2009)*. The classification was then compared with results from the back trajectory analysis (Figure 3) and satellite images described in section 2.2.
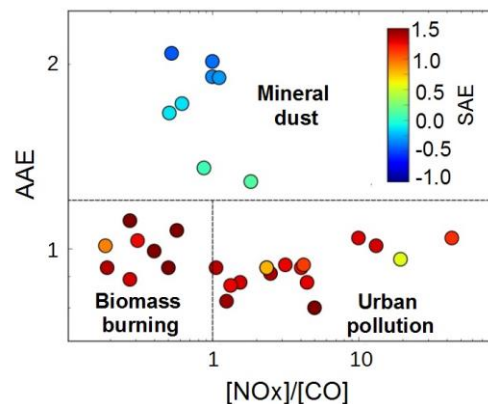
Figure 2. Absorption Ångström Exponent (AAE) as a function of the ratio NOx to CO. The markers are colored according to the Scattering Ångström Exponent (SAE). Classification of mineral dust, biomass burning and urban pollution particles has been added to the figure.

The guidelines for classification are as follows:

- *Anthropogenic pollution*: *SAE* was beyond threshold 0, indicating a large number fraction of small particles in urban plumes, and CO and NOx concentrations 2 times higher than the background concentrations. During the DACCIWA campaign background CO and NOx values were around 180 ppb and 0.28 ppb, respectively. The trajectories show large differences in the flow patterns and source regions with urban plumes originating from the polluted cities of Lomé, Accra and Abidjan. The aircraft sampling over land mostly followed the north-eastward direction (Figure 3d).

- *Biomass burning*: The criteria are the same as for urban pollution plumes except that trajectories track theses plumes back to active fire hotspots as observed by MODIS and the ratio NOx to CO was set below 1. CO and NOx are byproducts of combustion sources but CO is preserved longer along the plume when compared with NOx, which makes the ratio NOx to CO a good indicator for distinguishing fresh anthropogenic pollution plumes from biomass burning plumes transported

286   over long distances *(Wang et al., 2002; Silva et al., 2017)*. During this time of the year, most of the

287   forest and grassland fires were located in Central and Southern Africa (Figure 3a).

288   - *Mineral dust*: *AAE* higher than 1 indicates a large mass fraction of mineral dust and a *SAE* below

289   0 indicate a high effective particle diameter. The source region of the dust loaded air masses was

290   located in the Saharan desert and in the Sahel (Figure 3b).

291   - *Dust and biomass burning mixing:* Combining remote sensing observations and model

292   simulations, *Flamant et al. (2018a)* identified a biomass burning plume mixed with mineral dust.

293   This agrees well with the measured *AAE* of 1.2 and *SAE* of 0.3 observed in this layer. *Menut et al.*

294   *(2018)* have shown that one of the transport pathways of biomass burning aerosols from Central

295   Africa was associated with northward advection towards Chad and then westward displacement

296   linked to the African Easterly Jet. The plume originated from a broad active biomass burning area

297   including Gabon, the Republic of Congo and the Democratic Republic of Congo and passed over

298   areas with strong dust emissions further north within 1–3 days before being sampled by the aircraft

299   (Figure 3c).

300   - *Background:* We refer to background conditions as an atmospheric state in the boundary layer

301   without the detectable influence of mineral dust, biomass burning or local anthropogenic sources.

302   Most back trajectories originated from the marine atmosphere and coastal areas south of the

303   sampling area.
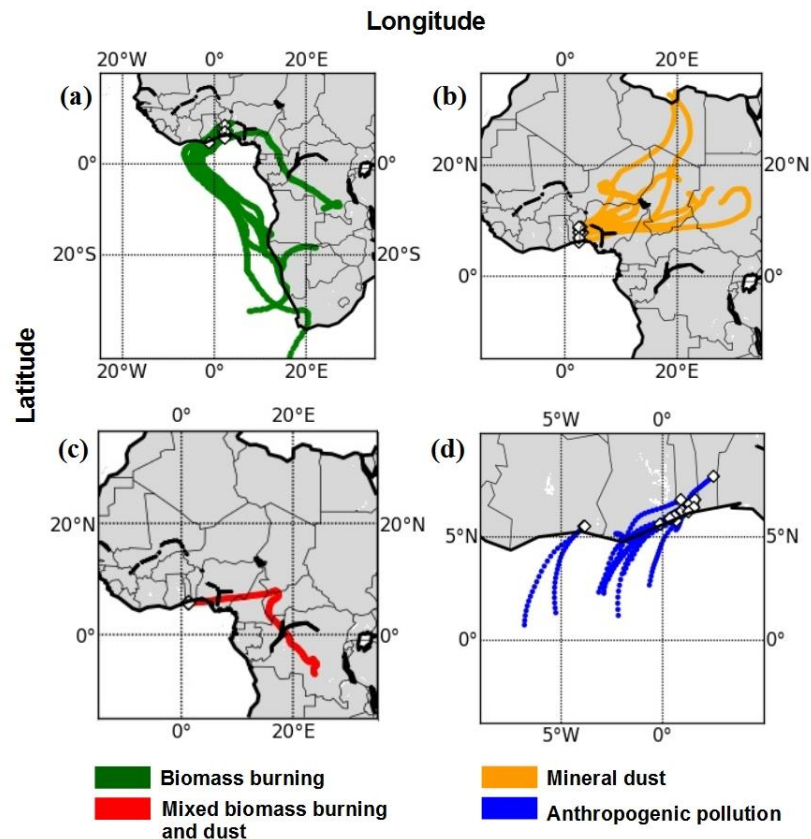
Biomass burning
Mixed biomass burning and dust
Mineral dust
Anthropogenic pollution

3.1. Aerosol vertical distribution

Figure 4 shows a statistical analysis of N_{fine}, N_{coarse} and σ_{ext} derived from the *in-situ* measurements of vertical profiles. The aerosol vertical structure is strongly related to the meteorological structure of the atmosphere (see *Knippertz et al., 2017* for an overview of the DACCIWA field campaign). Therefore wind vector and potential temperature profiles acquired with the aircraft have been added to Figure 4 as a function of the dominating aerosol composition, introduced in Figure 1. The data from individual vertical profiles were merged into 200 m vertical bins from the surface to 6 km amsl. The profiles were calculated using only individual profiles obtained outside of clouds.
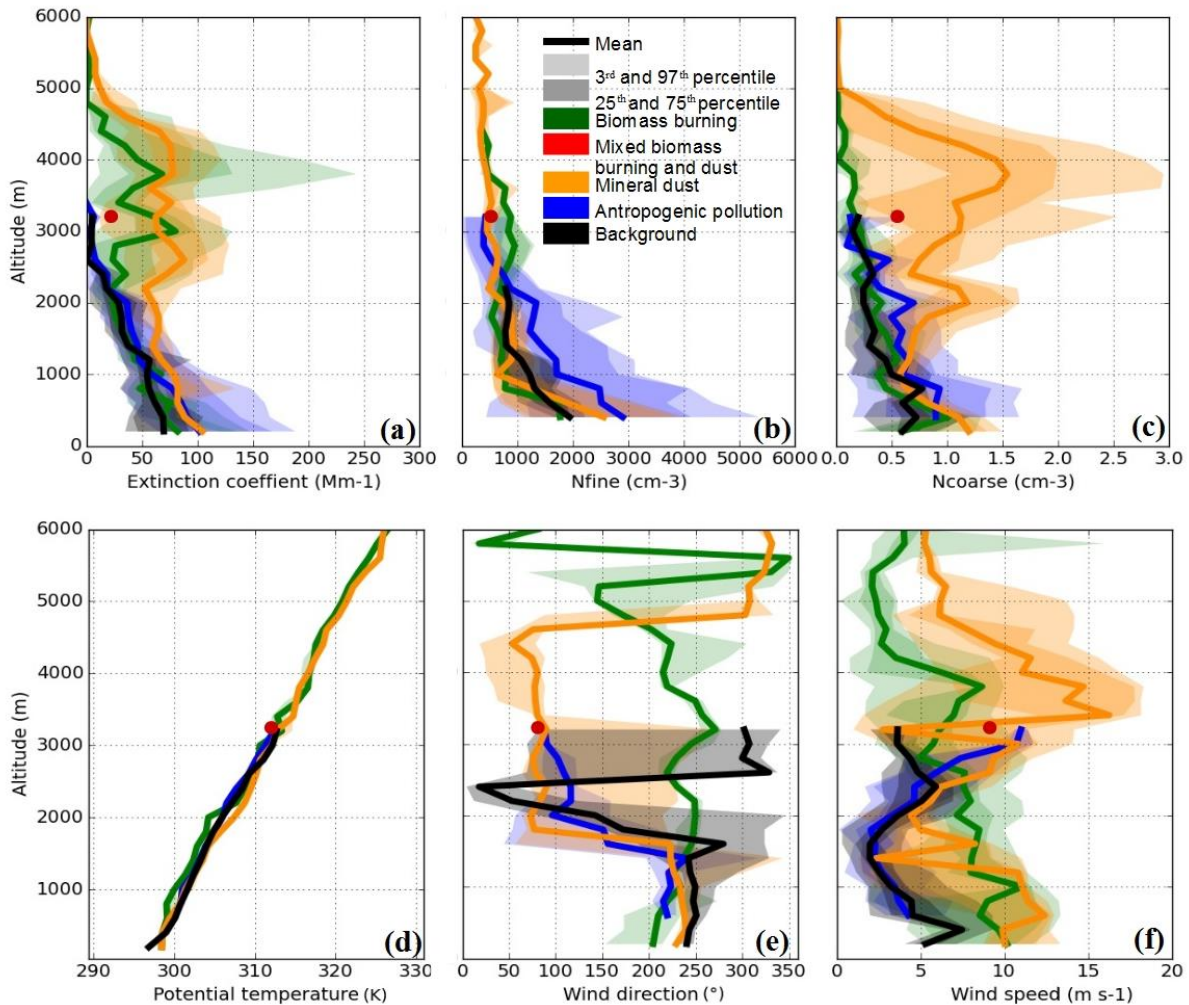
Figure 4. Vertical layering of aerosols and meteorological variables for profiles for which aerosols dominated by biomass burning (green), dust (orange), mixed dust-biomass burning (red), anthropogenic pollution (blue) and background particles (black) were detected. The panels show profiles of (a) the extinction coefficient at 530 nm, (b) the particle number

325

326   The observed wind profiles highlight the presence of several distinct layers in the lower

327   troposphere. For cases related to dust, urban pollution and background condition, we clearly

328   observe the monsoon layer up to 1.5 km amsl which is characterized by weak to moderate wind

329   speeds (2 to 10 m s^{-1}, the later corresponding to dust cases) and a flow from the southwest (220-

330   250°). In all three air mass regimes, the monsoon layer is topped by a 500 to 700 m deep layer

331   characterised by a sharp wind direction change (from south-westerly to easterly). Weak wind

332   speeds (less than 5 m s^{-1}) are observed in urban pollution and background conditions, while higher

333   wind speeds are observed in the dust cases. Above 2.5 km amsl, the wind speed increases in the

334   urban pollution and dust cases and the wind remains easterly, indicating the presence of the

335   African easterly jet with its core typically farther north over the Sahel (Figure 8 in *Knippertz et al.,*

336   *2017* for the latitudinal variations of the African easterly jet during the DACCIWA field phase).

337   The maximum easterlies are observed in the dust cases slightly below 3.5 km amsl (> 15 m s^{-1}).

338   For the background cases, the wind above the shear layer shifts to north-westerly and remains

339   weak (~i.e. 5 m s^{-1}). Overall, the wind profile associated with the biomass burning cases is quite

340   different from the other three cases, with a flow essentially from the south-southwest below 5 km

341   amsl and higher wind speeds in the lower 2 km amsl than above, and a secondary maximum of 7

342   m s^{-1} at 4 km amsl.

343

344   The vertical distribution of aerosol particles was very inhomogeneous, both across separate

345   research flights and between individual plumes encountered during different periods of the same

346   flight. Measurements of aerosols within this analysis cover a broad geographic region, as shown in

347   Figure 1, which may explain some of the variability. SWA is subject to numerous anthropogenic

348   emission sources (e.g. road traffic, heavy industries, open agriculture fires, etc.) coupled to

349   biogenic emissions from the ocean and forests. These resulting large emissions are reflected in the

350   high variability of σ_{ext}, N_{fine} and N_{coarse} in the lower troposphere over SWA. Below 2.5 km amsl, σ_{ext}

351   showed a large heterogeneity with values ranging from 35 to 188 Mm^{-1} between the 3rd and 97th

352   percentile and a median value of 55 Mm^{-1}. The variability of σ_{ext} values was slightly enhanced near

353   the surface and was correlated to N_{fine} and N_{coarse} which ranged from 443 to 5250 cm^{-3} and from

354   0.15 to 1.6 cm^{-3}, respectively. Maximum surface σ_{ext} was recorded in the anthropogenic pollution

355   plume of Accra where high N_{fine} was sampled. The aerosol vertical profile is strongly modified

356   during biomass burning and dust events. The dust plume extends from 2 to 5 km amsl, and is

357   associated with transport from the dust sources in Chad and Sudan (see Figure 3) with the midlevel

358   easterly flow. The biomass burning plume extends from 1.5 to 5 km amsl and is associated with

359   transport from the southwest in a layer of enhanced wind speed just below 4 km amsl as discussed

360   above. Both layers showed enhanced σ_{ext} with median values of 68 Mm^{-1} (p_{03} = 12 Mm^{-1}; p_{97} = 243

361   Mm^{-1}) in biomass burning plumes and 78 Mm^{-1} (p_{03} = 45 Mm^{-1}; p_{97} = 109 Mm^{-1}) in dust plumes.

362   As expected, the extinction profile was strongly correlated to N_{fine} for biomass burning layers and

363   N_{coarse} for dust layers.

364

365   A prominent feature in the vertical profiles is the presence of fine particles up to 2.5 km amsl

366   outside of biomass burning or dust events. σ_{ext}, N_{fine} and N_{coarse} continuously decrease with altitude,

367   most likely due to vertical mixing of local emissions from the surface to higher levels. Therefore,

368   the regional transport of locally emitted aerosols was not limited to the surface but occurred also at

369   higher altitude. Recently, numerical tracer experiments performed for the DACCIWA airborne

370   campaign period have demonstrated that a combination of land–sea surface temperature gradients,

371   orography-forced circulation and the diurnal cycle of the wind along the coastline favor the

372   vertical dispersion of pollutants above the boundary layer during daytime *(Deroubaix et al., 2019;*

373   *Flamant et al., 2018a)*. Because of these complex atmospheric dynamics, aerosol layers transiting

374   over the Gulf of Guinea in the free troposphere could be contaminated by background or urban

375   pollution aerosols from the major coastal cities.

376

377   **3.2. Aerosol size distribution**

378   Figure 5a shows the range of variability of the number and volume size distributions measured

379   during DACCIWA. These are extracted from the SLRs identified in Fig.1. Figure 5b shows the

380   same composite distribution normalized by CO concentration in order to account for differences in

381   the amount of emissions from combustion sources.

382
383
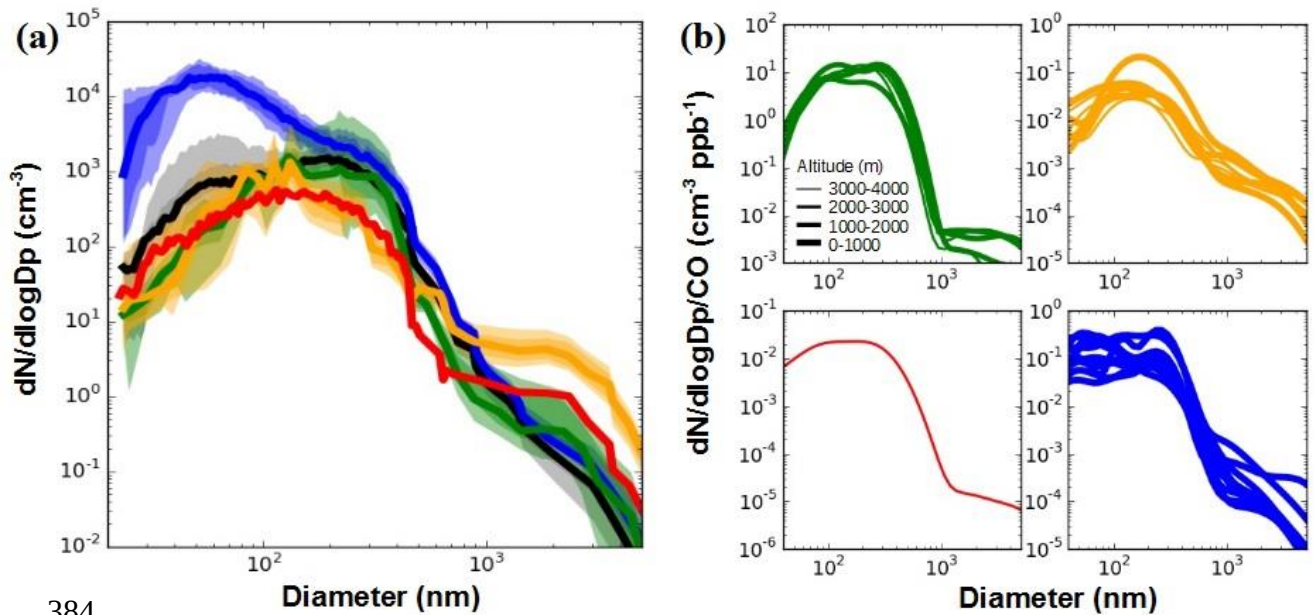
Figure 5. (a) Statistical analysis of number size distributions with colored areas representing the 3th, 25th, 75th and 97th percentiles of the data and (b) number size distributions normalized to CO for plumes dominated by biomass burning (green), dust (orange), mixed dust-biomass burning (red), anthropogenic pollution (blue) and background particles (black). In panel b, the line thickness is scaled by the altitude of the aerosol plume.

Considerable variability in the number concentration of the size distributions, up to approximately 2 orders of magnitude, was observed for a large fraction of the measured size range. The size distributions varied both for different aerosol types and for a given aerosol class. This reflects the relative wide range of different conditions that were observed over the region, both in terms of sources, aerosol loading, and lifetimes of plumes.

In particular for ultrafine particles with diameters below 100 nm, large differences are observed, with an increase as large as a factor of 50 in urban plumes, which reflects concentration increase from freshly formed particles. Interestingly elevated number concentrations of these small-diameter particles were also observed in some dust layers. Comparing the particle size distribution of the different dust plumes sampled during the field campaign, a variation as large as a factor of 20 in the number concentration of ultrafine particles is found (i.e. Figure 4). Their contribution decreased with height as reflected by higher small particle number recorded in dust plumes below 2.5 km amsl (Figure 4b and 5b). As the composite urban size distributions showed a relatively similar ultrafine mode centered at 50 nm, dust layers have most likely significant contributions from anthropogenic pollution aerosol freshly emitted in SWA. The ultrafine mode was not

407 observed in biomass burning size distributions, even though dust and biomass burning plumes
408 were sampled in the same altitude range. We interpret this observation with dust plumes
409 transported below 2.5 km amsl that were sampled over the region of Savè (8°01'N, 2°29'E; Benin)
410 near the identified urban air mass transported northeastwards from Lomé and/or Accra and which
411 may have collected significant fresh pollution on their way, whereas biomass burning plumes
412 collected at the same altitude and sampled over Ivory Coast south of the Abidjan pollution plumes
413 may not have been affected by significant direct pollution (Figure 1).

414

415 The accumulation mode was dominated by two modes centered at $D_{p,g}$ ~ 100 and 230 nm
416 depending on the aerosol plume. The particle size distributions for biomass burning plumes were
417 generally dominated by an accumulation mode centered at $D_{p,g}$ ~ 230 nm. Despite the relative wide
418 range of sources and lifetimes of the biomass burning plumes sampled throughout the campaign
419 (Figure 3), the $D_{p,g}$ in the accumulation mode showed little variation ($D_{p,g}$ from 210 to 270 nm)
420 between the plumes. Similarly, previous field studies found accumulation mode mean diameters
421 from 175 to 300 nm for aged biomass burning plumes, regardless of their age, transport time and
422 source location *(Capes et al., 2008; Janhäll et al., 2010; Weinzierl et al., 2011; Sakamoto et al.,*
423 *2015; Carrico et al. 2016)*. The coagulation rate can be very high in biomass burning plumes and
424 can shape the size distribution over a few hours (*Sakamoto et al., 2016*). It is worth noting that in
425 the biomass burning and dust size distributions there is a persistent particle accumulation mode
426 centered at ~100 nm that exceeds the amount of particles centered at 230 nm in some layers. This
427 small mode is unlikely to be related to long-range transport of biomass burning and Saharan dust
428 emissions, as it would be expected that particles in this size range would grow to larger particles
429 through coagulation relatively quickly. As similar concentrated accumulation modes of particles
430 have been observed in background plumes, it suggests the entrainment of background air from the
431 boundary layer in dust and biomass burning plumes.

432

433 The number concentration of large super-micron particles was strongly enhanced in the mineral
434 dust layers. The peak number concentration displayed a broad shape at $D_{p,g}$ ~ 1.8 µm, which is
435 comparable to literature values of other long-range transported dust aerosols *(Weinzierl et al.,*
436 *2011; Ryder et al., 2013; Denjean et al., 2016; Liu et al., 2018)*. The super-micron mode of the
437 dust plume is expected to be impacted by the mixing with other particles in case of an internal
438 mixing, which should somewhat increase the particle size. The relatively homogeneous $D_{p,g}$ in the
439 coarse mode of dust reported here ($D_{p,g}$ from 1.7 to 2.0 µm) suggests low internal mixing with
440 other atmospheric species. Besides, the volume size distribution in urban plumes showed

441   significant presence (~ 65% of the total aerosol volume) of large particles with diameters of ~ 1.5

442   – 2 µm, which were also observed in background conditions. We measured *AAE* in the range 0.7-1

443   in anthropogenic pollution plumes (Figure 2), which suggests negligible contribution of mineral

444   dust in these plumes. This coarse mode has most likely significant contributions from sea salt

445   particles, as plumes arriving from the cities were transported at low altitude over the ocean (Fig.

446   3).

447

448   3.3. Aerosol optical properties

449   *SSA* is one of the most relevant intensive optical properties because it describes the relative

450   strength of the aerosol scattering and absorption capacity and is a key input parameter in climate

451   models *(Solmon et al., 2008)*. Figure 6 shows the spectral *SSA* for the different SLRs considered in

452   this study.

453

Figure 6. (a) Statistical analysis of single scattering albedo at 450, 550 and 660 nm for plumes dominated by biomass burning (green), dust (orange), mixed dust-biomass burning (red), anthropogenic pollution (blue) and background particles (black). The boxes enclose the 25th and 75th percentiles, the whiskers represent the 5th and 95th percentiles and the horizontal bar represents the median. (b) Spectral SSA for the different individual plumes considered in this study. The mixed dust-biomass burning plume is represented by a dot because it is derived from measurements during only one SLR.

461

462   The highest absorption (lowest *SSA*) at all three wavelengths was observed for biomass burning

463   aerosols. *SSA* values ranged from 0.69–0.78 at 440 nm, 0.71–0.77 at 550 nm and 0.65–0.76 at 660

464   nm. This is on the low side of the range of values (0.73–0.93 at 550 nm) reported over West Africa

465   during DABEX for biomass burning plumes mixed with variable proportion of mineral dust

466   *(Johnson et al., 2008)*. No clear tendency was found for the spectral dependence of *SSA*, which in

467   some of the cases decreased with wavelength and in others were very similar to each other at all

468   three wavelengths.

469

470   *SSA* values of anthropogenic pollution aerosols were generally intermediate in magnitude with

471   median values of 0.81 at 440 nm, 0.82 at 550 nm and 0.82 at 660 nm. Our data show that the value

472   of *SSA* varied significantly for the different plumes. Some pollution aerosols absorb almost as

473   strongly as biomass burning aerosols with *SSA(550nm)* values as low as 0.72, whereas the highest

474   *SSA(550nm)* value observed was 0.86. In addition, the absorption properties of urban aerosol

475   varied greatly between the sampled plumes for smoke of apparent same geographic origin. For

476   example, we measured *SSA(550nm)* values from 0.72 to 0.82 in the Accra pollution outflow. The

477   variability in SSA values may be due to the possible contribution of emissions from different cities

478   to the sampled pollution plumes (*Deroubaix et al., 2019)*, thus having different combustion

479   sources and chemical ages. Past in-situ measurements of aerosol optical properties over SWA cities

480   appear, unfortunately, to be absent from literature. However, the flat spectral dependence of SSA

481   appears to be anomalous for anthropogenic pollution aerosols, as SSA has been shown to decrease

482   with increasing wavelength for a range of different urban pollution plumes over European,

483   American and Asian cities (*Dubovick et al., 2002; Di Biagio et al., 2016; Shin et al., 2019).*

484

485   The magnitude of *SSA* increased at the three wavelengths when dust events occurred. Large

486   variations in *SSA* were obtained with values ranging from 0.76–0.92 at 440 nm, 0.81–0.94 at 550

487   nm and 0.81–0.97 at 660 nm. The measurement of *SSA* is highly dependent on the extent to which

488   the coarse mode is measured behind the aerosol sampling inlet. *Denjean et al. (2016)* found that

489   the absolute error associated with *SSA, g and MEE* of dust aerosols due to the CAI inlet is in the

490   range covered by the measurement uncertainties. However, different aerosol inlet systems were

491   used during previous field campaigns, which makes comparison of our results with previous

492   measurements difficult. Overall, compared with the literature for transported dust, lower values

493   were obtained in the present study for few cases. For example, *Chen et al. (2011)* reported

494   SSA(550 nm) values of 0.97±0.02 during NAMMA (a part of AMMA operated by NASA) using

495   an inlet with a comparable sampling efficiency. The lower values from DACCIWA reflect

496   inherently more absorbing aerosols in some dust plumes. In contrast to fire plumes, the SSA of

497   dust aerosol showed a clear increasing trend with wavelength. This behavior is likely due to the

498   domination of large particles in dust aerosol, which is in agreement to similar patterns observed in

 dust source regions (*Dubovik et al., 2002)*. Moreover, an increase of SSA is observed with

500 wavelength for mixed dust-smoke aerosol, suggesting that the aerosol particles were

501 predominantly from dust, albeit mixed with a significant loading of biomass burning.

502

		SSA(450)	SSA(550)	SSA(660)	MEE(450)	MEE(550)	MEE(660)	g(450)	g(550)	g(660)	SAE
Mineral dust	median	0.88	0.90	0.93	0.74	0.68	0.66	0.74	0.72	0.69	-0.35
	3th	0.82	0.82	0.86	0.38	0.38	0.39	0.69	0.67	0.65	-0.56
	25th	0.85	0.87	0.90	0.43	0.43	0.43	0.73	0.72	0.67	-0.48
	75th	0.91	0.93	0.96	0.94	0.85	0.85	0.75	0.74	0.72	-0.25
	97th	0.92	0.95	0.97	1.57	1.37	1.21	0.78	0.76	0.72	-0.12
Biomass burning	median	0.74	0.76	0.72	1.91	1.62	1.34	0.69	0.68	0.61	1.07
	3th	0.70	0.72	0.66	0.94	1.45	1.22	0.64	0.65	0.59	0.59
	25th	0.70	0.76	0.71	1.67	1.48	1.27	0.69	0.65	0.60	0.83
	75th	0.77	0.77	0.74	1.86	1.65	1.55	0.72	0.68	0.62	1.15
	97th	0.78	0.77	0.76	2.38	1.92	1.58	0.73	0.68	0.63	1.64
Mixed dust-Biomass burning	median	0.76	0.77	0.81	1.58	1.40	1.30	0.73	0.66	0.64	0.38
	3th	-	-	-	-	-	-	-	-	-	-
	25th	-	-	-	-	-	-	-	-	-	-
	75th	-	-	-	-	-	-	-	-	-	-
	97th	-	-	-	-	-	-	-	-	-	-
Anthropogenic Pollution	median	0.83	0.84	0.85	2.60	2.49	1.90	0.60	0.61	0.62	0.75
	3th	0.78	0.79	0.81	0.70	1.24	0.54	0.60	0.59	0.54	0.30
	25th	0.80	0.82	0.83	2.14	2.25	1.53	0.62	0.60	0.56	0.65
	75th	0.84	0.86	0.85	3.51	2.96	2.53	0.69	0.62	0.67	0.89
	97th	0.87	0.88	0.90	3.70	4.83	2.74	0.73	0.64	0.70	0.94

503
504 **Table 2. Single scattering albedo, extinction mass efficiency, asymmetry parameter, single**
505 **scattering albedo and scattering Ångstrom exponent for the dominant aerosol classification.**
506
507 As shown in Table 2, the observed variability of *SSA* reflects a large variability for *MEE* at 550nm,

508 which spans a wide range from 0.38 to 1.37 $m^2\ g^{-1}$, 1.45 to 1.92 $m^2\ g^{-1}$ and 1.24 to 4.83 $m^2\ g^{-1}$ for

509 dust, biomass burning for anthropogenic polluted aerosols, respectively. *MEE* is heavily influenced

510 by the mass concentrations in the accumulation mode where the aerosol is optically more efficient

511 in extinguishing radiation. We found *MEE* to be positively correlated with *SAE* (not shown), which

512 was expected because of the dependence of *MEE* on particle size. In contrast, the values of *g*

513 appear to differ only little between the sampled plumes for a given aerosol class. We found *g* in the

514 range of 0.67–0.76 for dust, 0.65–0.68 for biomass burning and 0.59–0.64 for anthropogenic

515 polluted aerosols at 550 nm. *g* values in dust plumes were high, which is expected due to the

516 presence of coarse particles contributing to forward scattering.

517

518   This analysis includes sampled aerosols originating from different source regions and having
519   undergone different aging and mixing processes, which could explain some of the variability. The
520   impact of these factors on the magnitude and spectral dependence of optical parameters will be
521   investigated in the following section.
522

523   **4. Discussion**
524   **4.1. Contribution of local anthropogenic pollution on aerosol absorption properties**
525   Figure 7 shows the vertical distribution of *SSA, SAE* and *NOx* mixing ratio for the dominant
526   aerosol classification. We exclusively consider measurements acquired during SLRs, since only
527   during these phases the whole set of aerosol optical properties were measured. In dust plumes, if
528   we exclude the case of mixing with biomass burning aerosol, SSAs were fairly constant above 2.5
529   km amsl with values ranging between 0.90 and 0.93 at 550 nm, in agreement with values reported
530   over dust source regions *(Schladitz et al., 2009; Formenti et al., 2011; Ryder et al., 2013, 2018)*.
531   Despite the range of sources identified during DACCIWA, dust absorption properties do not seem
532   to be clearly linked to particle origin or time of transport. Aerosols were more absorbing within the
533   low-altitude dust plumes with SSA values dropping to 0.81. *SAE* values exhibited simultaneously a
534   sharp increase close to zero below 2.5 km amsl. This is consistent with a higher concentration of
535   fine particles, though the value of *SAE* was still much lower than for pollution or background
536   aerosol (i.e. where it is typically > 0.2), which means that scattering was still dominated by larger
537   particles. Based on these observations, the strong variation in the light-absorption properties of
538   dust-dominated aerosol over SWA could be attributed to the degree of mixing into the vertical
539   column with either freshly emitted aerosols from urban/industrial sources or long-range
540   transported biomass burning aerosol.
541

542   One of the critical factors in the calculation of aerosol direct and semi-direct radiative effects is the
543   mixing state of the aerosols, which can significantly affect absorbing properties. There were no
544   direct observational constraints available on this property during the DACCIWA airborne
545   campaign. However, we investigated the probable aerosol mixing state by calculating composite
546   SSA from the aerosol size distribution. On the basis of Figure 5, dust size distribution showed only
547   minor discrepancies in the mean and standard deviation of the coarse mode but significant
548   differences in the balance between fine and coarse modes, which suggests low internal mixing of
549   dust with other atmospheric species. The size distributions of mixed dust-pollution have been
550   deconvoluted by weighting the size distributions of mineral dust and anthropogenic pollution
551   aerosol averaged over the respective flights. This assumes that dust was externally mixed with the

552 anthropogenic pollution particles and assumes a homogeneous size distribution for the dust and
553 anthropogenic pollution aerosol throughout a flight. σ_{scat} and σ_{abs} were then calculated using Mie
554 theory from each composite size distributions and the corresponding k and m. The refractive
555 indices at 550 nm were assumed to be 1.52-0.002i and 1.60-0.040i for dust and anthropogenic
556 pollution particles, respectively, which are the mean values deduced from the data inversion
557 procedure (i.e. section 2.3.1) throughout the campaign. The resulting σ_{scat} and σ_{abs} were used to
558 calculate a composite *SSA*. A similar calculation was performed for the mixed dust-biomass
559 burning case. Figure 7 shows a good agreement with the observations of *SSA*, implying that
560 external mixing appears to be a reasonable assumption to compute aerosol direct and semi-direct
561 radiative effects in these dust layers for modeling applications. This is consistent with the filter
562 analysis performed during AMMA and SAMUM-2, which did not reveal any evidence of internal
563 mixing in both mixed dust-biomass burning and dust-anthropogenic pollution layers *(Chou et al.,*
564 *2008; Lieke et al., 2011; Petzold et al., 2011).*

565
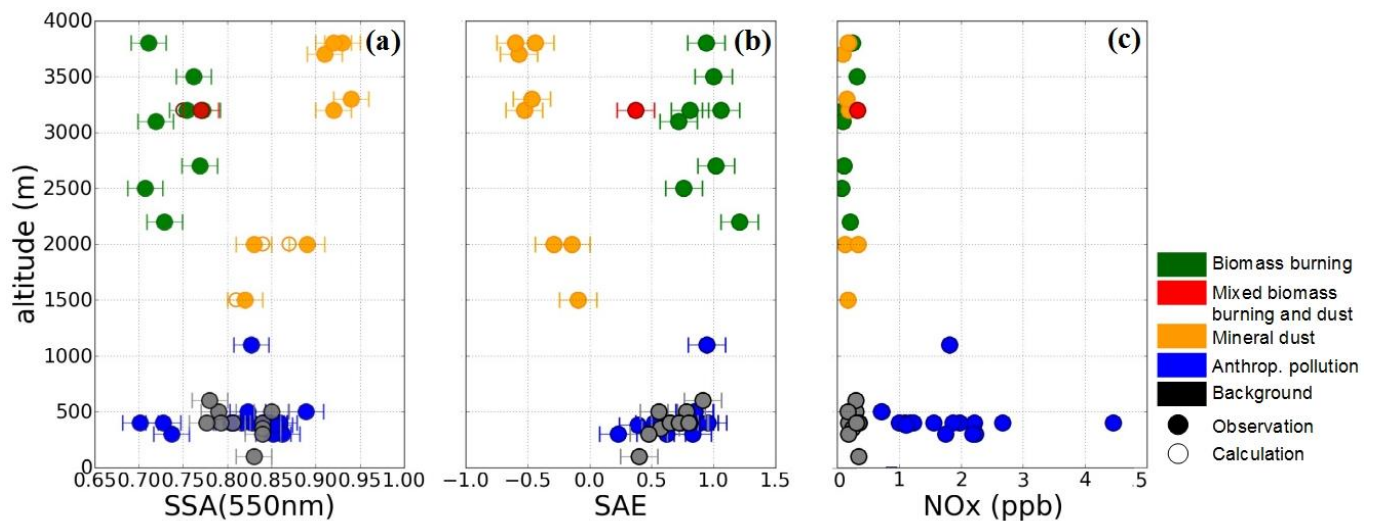
566 **Figure 7. Vertical distribution of (a) the single scattering albedo at 550 nm, (b) the scattering**
567 **Ångstrom exponent and (c) NOx mixing ratio for the dominant aerosol classification. In**
568 **panel (a), full circles represent *SSA* measurements and empty circles represent composite**
569 ***SSA* calculated by deconvoluting size distribution measurements in mixed dust layers and**
570 **assuming an external mixing state.**

571
572 *SSA*, *SAE* and NOx of biomass burning plumes did not significantly vary with height from 2.2 to
573 3.8 km amsl. Moreover, the size distribution of biomass burning aerosols for the observed cases
574 did not show significant contribution of ultrafine particles (Figure 5). These observations seem to
575 indicate that the absorption properties of biomass burning plumes were not affected by direct
576 pollution emissions/

578   In the boundary layer, the similar *SSA* and *SAE* in anthropogenic pollution and background plumes
579   suggests that background aerosol may be rather called background pollution originating from a
580   regional background source in the far field. Our analysis of the spectral dependence of *SSA*
581   showed no apparent signature of anthropogenic pollution aerosols (see section 3.3) despite a strong
582   increase of aerosol number concentrations in air masses crossing urban centers (see section 3.2).
583   This can be explained by two factors: First, the majority of accumulation mode particles were
584   present in the background, while the large proportion of aerosols emitted from cities resided in the
585   ultrafine mode particles that have less scattering efficiencies (Figure 5). Second, large amounts of
586   absorbing aerosols in the background can minimize the impact of further increase of absorbing
587   particles to the aerosol load. The high CO values (~180 ppb) observed in background conditions
588   further indicates a strong contribution of combustion emissions at the surface. Recent studies
589   showed a large background of biomass burning transported from the Southern Hemisphere in SWA
590   that dominated the aerosol chemical composition in the boundary layer *(Menut et al., 2018;*
591   *Haslett et al., 2019)*. The high absorbing properties (*SSA*~0.81 at 550nm) and the presence of
592   particles both in the accumulation and super-micron modes (i.e. section 3.2.) in background
593   plumes are consistent with being a mixture of aged absorbing biomass burning and Atlantic marine
594   aerosol. These results highlight that aerosol optical properties at the surface were dominated by the
595   widespread biomass burning particles at regional scale.

596

597   **4.2. Aging as a driver for absorption enhancement of biomass burning aerosol**
598   The optical properties of aerosols are determined by either the aerosol chemical composition, the
599   aerosol size distribution, or both. Changes in the size distribution of biomass burning aerosol due
600   to coagulation and condensation have been shown to alter the *SSA*, as particles increase towards
601   sizes for which scattering is more efficient *(Laing et al., 2016)*. Variations in particle chemical
602   composition, caused by source emissions and aging processes associated with gas-to-particle
603   transformation and internal mixing, has been shown to change the *SSA (Abel et al., 2003; Petzold*
604   *et al., 2011)*.

605

606   In order to determine the contributions from size distribution and chemical composition to the
607   variation of *SSA* in biomass burning plumes, *SSA* is presented as a function of *SAE* and *k* in Figure
608   7a and b, respectively. *k* was iteratively varied to reproduce the experimental scattering and
609   absorption coefficients, as described in section 2.3.1. It appears that the variation of the size
610   distribution (assessed via *SAE* in Figure 8a) had minimal impact in determining the variability of

611   *SSA*. Thus, the observations suggest that there was no effect of plume age on the size distribution,

612   consistent with previous observations of size distribution in aged North American biomass

613   burning plumes *(Sakamoto et al., 2015; Carrico et al., 2016; Laing et al., 2016)*. Using a

614   Lagrangian microphysical model, *Sakamoto et al. (2015)* have shown a rapid shift to larger sizes

615   for biomass burning plumes within the first hours of aging. Less drastic but similarly rapid growth

616   by coagulation was seen by *Capes et al. (2008)* in their box model. Given that the biomass burning

617   plumes sampled during DACCIWA had more than 5 days in age, the quick size-distribution

618   evolution within the early plume stages might explain the limited impact of the size distribution on

619   the *SSA*.
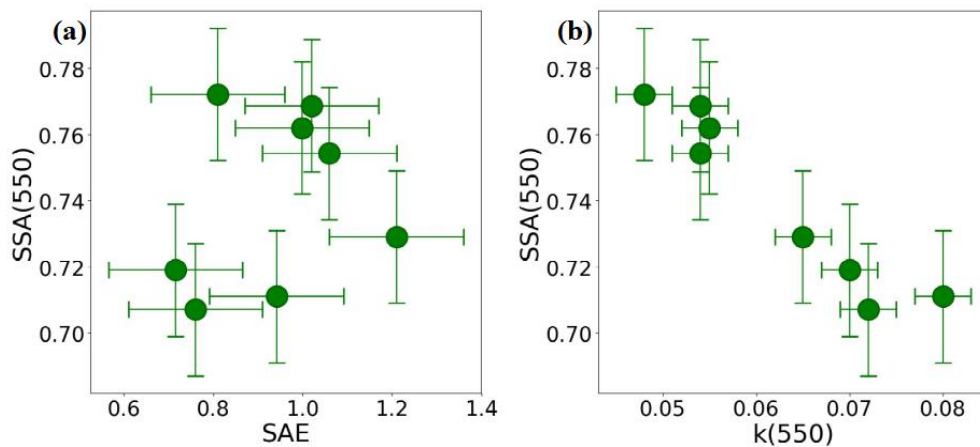
620
621   **Figure 8. Contribution to single scattering albedo (a) from particle size (assessed via *SAE*)**
622   **and (b) from composition (assessed via *k*) in biomass burning plumes.**
623

624   In contrast, Figure 8b shows that there was a consistent decrease in *SSA* with increasing *k*,

625   although there is some variability between the results from different plumes. The observed

626   variability of *SSA* is reflected in a large variability of *k*, which is estimated to span the large range

627   0.048–0.080 at 550 nm. k depends both on the aerosol chemical composition and size distribution

628   *(Mita and Isono, 1980)*. Given that *SSA* was found to be independent of the aerosol size

629   distribution (Figure 8a), Figure 8b suggests that *SSA* variability was strongly influenced by the

630   variability in composition of biomass burning aerosol, implying a high contribution for light-

631   absorbing particles. No clear tendency was found for the wavelength dependence of *k*, which in

632   some of the cases increases with wavelength and in others decreases (not shown).

633   Correspondingly, values of *AAE* in biomass burning plumes ranged from 0.9 to 1.1 with a median

634   value of 1.0. Theoretically, fine-mode aerosol with absorption determined exclusively by BC

635 would have *AAE* equal to 1.0, since BC is expected to have a spectrally constant *k (Bond et al.,*
636 *2013)*. Therefore, the low *SSA* values observed in biomass burning plumes over SWA and the
637 small spectral variation of *k* both suggest that BC is the dominant absorber in the visible and near-
638 IR wavelengths for these biomass burning aerosols.

639

640 Compared with past in-situ measurements of aged biomass burning aerosol, *SSA* values over SWA
641 (0.71–0.77 at 550 nm) are at the lower end of those reported worldwide (0.73–0.99 at 550 nm)
642 *(Maggi et al., 2003; Reid et al. 2005; Johnson et al., 2008; Corr et al. 2012; Laing et al. 2016)*.
643 This can be attributed in part to the high flaming versus smoldering conditions of African smoke
644 producing more BC particles *(Andreae and Merlet, 2001; Reid et al., 2005)*, which inherently have
645 low *SSA* compared to other regions *(Dubovick et al*. 2002). However, *SSA* values over SWA are
646 significantly lower than the range reported near emission sources in sub-Saharan Africa and over
647 the southeast Atlantic, where values span over 0.84–0.90 at 550 nm *(Haywood et al., 2003b;*
648 *Pistone et al., 2019)*. Recent observations carried out on Ascension Island to the south-west of the
649 DACCIWA region showed that smoke transported from Central and South African fires can be
650 very light absorbing over the July-November burning season but *SSA* values were still higher
651 (0.80±0.02 at 530 nm; *Zuidema et al., 2018*) than those reported over SWA. A possible cause of
652 the lower *SSA* in SWA is that Ascension Island is much closer to the local sources and the aerosol
653 is therefore less aged.

654

655 Currently there are few field measurements of well-aged biomass burning emissions. Our
656 knowledge of biomass burning aerosol primarily comes from laboratory experiments and near-
657 field measurements taken within a few hours of a wildfire *(Abel et al., 2003; Yokelson et al., 2009;*
658 *Adler et al., 2011; Haywood et al., 2003b; Vakkari et al., 2014; Zhong and Jang, 2014; Forrister*
659 *et al., 2015; Laing et al., 2016; Zuidema et al., 2018)*. Exception made of the study by *Zuidema et*
660 *al. (2018)* over the southeast Atlantic, it is generally found that the aged biomass burning aerosol
661 particles are less absorbing than freshly emitted aerosols due to a combination of condensation of
662 secondary organic species and an additional increase in size by coagulation. This is in contrasts to
663 our results showing that *SSA* of biomass burning aerosols were significantly lower than directly
664 after emission and that the evolution of *SSA* occurred long time after emission.

665

666 There are three possible explanations for these results. First, one must consider sample bias. As
667 regional smoke ages, it can be enriched by smoke from other fires that can smolder for days
668 producing large quantities of non-absorbing particles, thereby increasing the mean *SSA (Reid et al.,*

669   *2005; Laing et al., 2016).* However, during DACCIWA, biomass burning plumes were transported
670   over the Atlantic Ocean and were probably less influenced by multiple fire emissions. Second,
671   there is evidence that fresh BC particles become coated with sulfate and organic species as the
672   plume ages in a manner that enhances their light absorption *(Lack et al., 2012; Schwarz et al.,*
673   *2008).* Finally, organic particles produced during the combustion phase can be lost during the
674   transport through photobleaching, volatilization and/or cloud-phase reactions *(Clarke et al., 2007;*
675   *Lewis et al., 2008; Forrister et al., 2015)*, which is consistent with the low *SSA* and *AAE* values we
676   observed. Assessing whether these aging processes impact the chemical components and
677   henceforth optical properties of transported biomass burning aerosol would need extensive
678   investigation of aerosol chemical composition that will be carried out in a subsequent paper.
679

680   5. Conclusions

681   This paper provides an overview of *in-situ* airborne measurements of vertically resolved aerosol
682   optical properties carried out over SWA during the DACCIWA field campaign in June-July 2016.
683   The peculiar dynamics of the region lead to a chemically complex situation, which enabled
684   sampling various air masses, including long-range transport of biomass burning from Central
685   Africa and dust from Sahelian and Saharan sources, local anthropogenic plumes from the major
686   coastal cities, and mixtures of these different plumes. This work fills a research gap by providing,
687   firstly, key climate relevant aerosol properties *(SSA, MEE, g, SAE, AAE)* and secondly,
688   observations of the impact of aging and mixing processes on aerosols optical properties.
689

690   The aerosol vertical structure was very variable and mostly influenced by the origin of air mass
691   trajectories. While aerosol extinction coefficients generally decreased with height, there were
692   distinct patterns of profiles during dust and biomass burning transport to SWA. When present,
693   enhanced values of extinction coefficient up to 240 Mm^{-1} were observed in the 2–5 km amsl range.
694   These elevated aerosol layers were dominated by either dust or biomass burning aerosols, which is
695   consistent with what would be expected on the basis of the atmospheric circulations during the
696   monsoon season *(McConnell et al., 2008; Knippertz et al., 2017)*. However, during one flight a
697   mixture of dust and biomass burning was found in a layer at around 3 km amsl, implying that there
698   may be substantial variability in the idealized picture. In the lower troposphere, the large
699   anthropogenic pollution plumes extended as far as hundreds of kilometers from the cities emission
700   sources and were not limited to the boundary layer but occurred also at higher levels up to 2.5 km
701   amsl, which is explained by vertical transport and mixing processes, partly triggered by the
702   orography of SWA (*Deroubaix et al., 2019; Flamant et al., 2018a).* The analysis of the aerosol size

703 distributions, *SAE* and NOx suggests a strong mixing of dust with anthropogenic pollution
704 particles in dust layers transported below 2.5 km amsl, whereas biomass burning plumes that were
705 transported more northward were not affected by this mixing. Both transport pathways and vertical
706 structures of biomass burning and dust plumes over SWA appear to be the main factors affecting
707 the mixing of anthropogenic pollution with dust and biomass burning particles.

708

709 The aerosol light absorption in dust plumes was strongly enhanced as the result of this mixing. We
710 find a decrease of *SSA(550nm)* from 0.92 to 0.81 for dust affected by anthropogenic pollution
711 mixing compared to the situation in which the dust plumes moved at higher altitudes across SWA.
712 Comparison of the particle size distributions of the different dust plumes showed a large
713 contribution of externally mixed fine mode particles in mixed layers, while there was no evidence
714 for internal mixing of coarse particles. Concurrent optical calculations by deconvoluting size
715 distribution measurements in mixed layers and assuming an external mixing state allowed to
716 reproduce the observed *SSA*s. This implies that an external mixing would be a reasonable
717 assumption to compute aerosol direct and semi-direct radiative effects in mixed dust layers.

718

719 Despite a strong increase of aerosol number concentration in air masses crossing urban
720 conglomerations, the magnitude of the spectral *SSA*s was comparable to the background.
721 Enhancements of light absorption properties were seen in some pollution plumes, but were not
722 statistically significant. A persistent spectral signature of biomass burning aerosols in both
723 background and pollution plumes highlights that the aerosol optical properties in the boundary
724 layer were strongly affected by the ubiquitous biomass burning aerosols transported from Central
725 Africa *(Menut et al., 2018; Haslett et al., 2019).* The large proportion of aerosols emitted from the
726 cities of Lomé, Accra and Abidjan that resided in the ultrafine mode particles have limited impact
727 on already elevated amounts of accumulation mode particles having a maximal absorption
728 efficiency. As a result, in the boundary layer, the contribution from local city emissions to aerosol
729 optical properties were of secondary importance at regional scale compared with this large
730 absorbing aerosol mass. While local anthropogenic emissions are expected to rise as SWA is
731 currently experiencing major economic and population growth, there is increasing evidence that
732 climate change is increasing the frequency and distribution of fire events *(Joly et al., 2015).* In
733 terms of future climate scenarios and accompanying aerosol radiative forcing, whether the large
734 biomass burning events that occur during the monsoon season would limit the radiative impact of
735 increasing anthropogenic emissions, remains an open and important question.

736

737   The *SSA* values of biomass burning aerosols transported in the free troposphere were very low
738   (0.71–0.77 at 550 nm) and have only rarely been observed in the atmosphere. The variability in
739   *SSA* was mainly controlled by the variability in aerosol composition (assessed via *k*) rather than by
740   variations in the aerosol size distribution. Correspondingly, values of *AAE* ranged from 0.9 to 1.1,
741   suggesting that BC particles were the dominant absorber in the visible for these biomass burning
742   aerosols. In recent years the southern Atlantic Ocean, especially the area of the west coast of
743   Africa, became an increasing focus in the research community, through the ORACLES/LASIC
744   (ObseRvations of Aerosols above CLouds and their intEractionS/Layered Atlantic Smoke
745   Interactions with Clouds), AEROCLO-sA (AErosol RadiatiOn and CLOuds in Southern Africa –
746   AEROCLO-SA) and CLARIFY (Cloud and Aerosols Radiative Impact and Forcing) projects
747   *(Zuidema et al.; 2016; Zuidema et al.; 2018; Formenti et al.; 2019)*. Comparison with literature
748   showed a consistent picture of increasing absorption enhancement of biomass burning aerosol
749   from emission to remote locations. Further, the range of *SSA* values over SWA was slightly lower
750   than that reported on Ascension Island to the south-west of the DACCIWA region, which
751   underscores that the evolution of *SSA* occurred long time after emission. While the mechanism
752   responsible for this phenomenon warrants further study, our results support the growing body of
753   evidence that the optical parameters used in regional/global climate modeling studies, especially
754   absorption by biomass burning aerosols, have to be better constrained using these recent
755   observations to determine the direct and semi-direct radiative effects of smoke particles over this
756   region *(Mallet et al. 2019)*. In particular and regarding the very high absorbing properties of
757   smoke, specific attention should be dedicated to the semi-direct effect of biomass burning aerosols
758   at the regional scale and its relative contribution to the indirect radiative effect.

759

760   We believe the set of DACCIWA observations presented here is representative of the regional
761   mean and variability in aerosol optical properties that can be observed during the monsoon season
762   over SWA, as the main dynamical features were in line with climatology *(Knippertz et al., 2017)*.
763   This is why results from the present study will serve as input and constraints for climate modeling
764   to better understand the impact of aerosol particles on the radiative balance and cloud properties
765   over this region and also will substantially support remote sensing retrievals.

Data availability.

All data used in this study are publicly available on the AERIS Data and Service Center, which can be found at http://baobab.sedoo.fr/DACCIWA.

Author contributions.

CD conducted the analysis of the data and wrote the paper. CD, TB, FB, NM, AC, PD, JB, RD, KS and AS operated aircraft instruments and processed and/or quality-controlled data. MM provided expertise on aerosol-climate interaction processes. CF and PK were PIs, who led the funding application and coordinated the DACCIWA field campaign. All co-authors contributed to the writing of the paper.

Acknowledgements.

The research leading to these results has received funding from the European Union 7th Framework Programme (FP7/2007-2013) under Grant Agreement no. 603502 (EU project DACCIWA: Dynamics-aerosol-chemistry-cloud interactions in West Africa). The European Facility for Airborne Research (EUFAR, http://www.eufar.net/) also supported the project through the funding of the Transnational Activity project OLACTA and MICWA. We thank the Service des Avions Français Instrumentés pour la Recherche en Environnement (SAFIRE, a joint entity of CNRS, Météo-France, and CNES) and operator of the ATR-42 for their support during the aircraft campaign. Cyrielle Denjean thanks CNES for financial support. The authors would like to thank Bruno Piguet (CNRM) and Michel Ramonet (LSCE) for their support in the data processing.

787 **Appendix 1. Summary of flight information. All flights were conducted during 2016.**

Flight number	Date	Take off time (UTC)	Landing time (UTC)	Events observed
F17	29 June	14:17	17:10	Export of pollution from Lomé
F18	30 June	12:52	16:29	Export of pollution from Lomé
F19	1 July	10:35	14:06	Export of pollution from Accra
F20	2 July	09:53	13:21	Export of pollution from Lomé Dust outbreak
F21	2 July	15:04	18:29	Export of pollution from Lomé Biomass burning outbreak Mixed dust-biomass burning outbreak
F22	3 July	09:54	13:29	Export of pollution from Lomé
F24	6 July	07:17	11:03	Export of pollution from Abidjan
F27	8 July	05:52	09:28	Export of pollution from Accra
F28	8 July	10:53	14:22	Dust outbreak
F29	10 July	10:31	14:11	Export of pollution from Lomé Dust outbreak
F30	11 July	07:19	11:01	Export of pollution from Abidjan Biomass burning outbreak
F31	11 July	13:48	16:42	Biomass burning outbreak
F32	12 July	13:56	17:20	Export of pollution from Accra
F33	13 July	12:40	16:11	Biomass burning outbreak
F35	15 July	09:32	13:00	Export of pollution from Lomé

788

789 **Appendix 2. Data inversion procedure to calculate the aerosol microphysical and optical**

790 **parameters.**

791
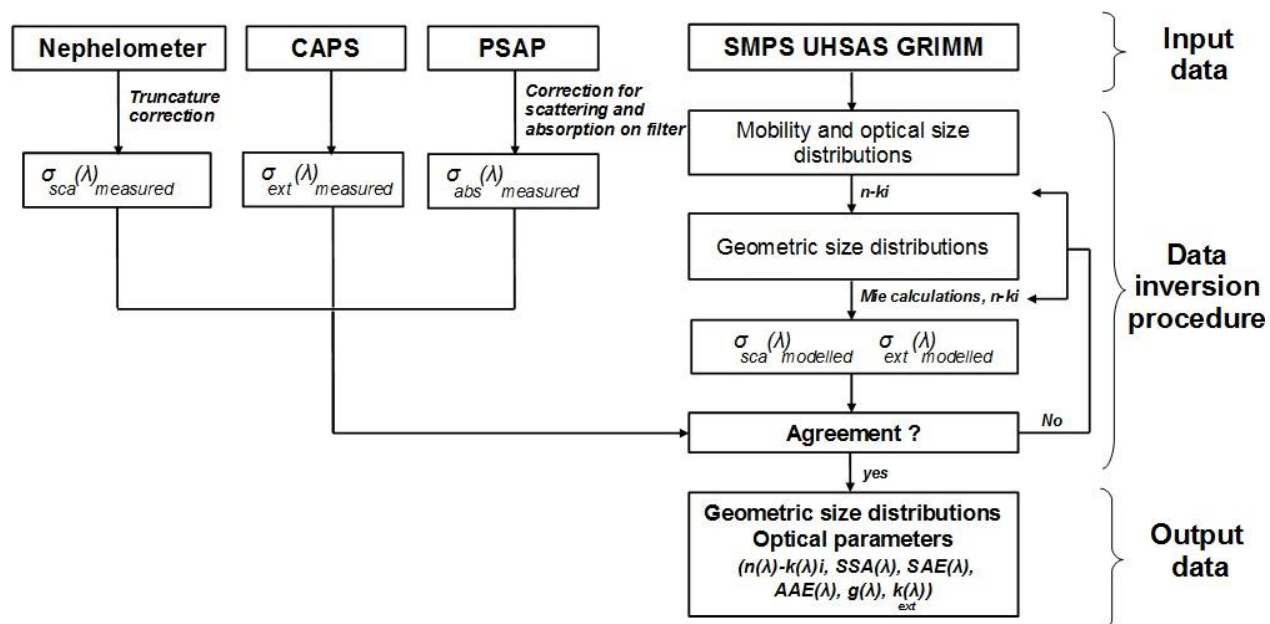
792 **References**

793 Abel, S. J., Haywood, J. M., Highwood, E. J., Li, J., and Buseck,P. R.: Evolution of biomass
794   burning aerosol properties from anagricultural fire in southern Africa, Geophys. Res. Lett., 30,
795   1783, doi:10.1029/2002GL017342, 2003.

796 Adler, G., Flores, J. M., Abo Riziq, A., Borrmann, S., and Rudich, Y., Chemical, physical, and
797   optical evolution of biomass burning aerosols: a case study, Atmos. Chem. Phys., 11, 1491-
798   1503, https://doi.org/10.5194/acp-11-1491-2011, 2011.

799 Andreae, M.O. and Merlet, P., Emission of Trace Gases and Aerosols from Biomass Burning.
800   Global Biogeochemical Cycles, 15, 955-966 , 2001.

801 Ansmann, A., Petzold, A., Kandler, K., Tegen, I. N. A., Wendisch, M., Müller, D., Weinzierl, B.,
802   Müller, T., and Heintzenberg, J.: Saharan Mineral Dust Experiments SAMUM–1 and
803   SAMUM–2: what have we learned?, Tellus B, 63, 403-429, doi: 10.1111/j.1600-
804   0889.2011.00555.x, 2011.

805 Bond, T. C., Doherty, S. J., Fahey, D. W., Forster, P. M., Berntsen,T., DeAngelo, B. J., Flanner, M.
806   G., Ghan, S., Kärcher, B., Koch,D., Kinne, S., Kondo, Y., Quinn, P. K., Sarofim, M. C.,
807   Schultz,M. G., Schulz, M.,Venkataraman, C., Zhang, H., Zhang, S., Bellouin,N., Guttikunda, S.
808   K., Hopke, P. K., Jacobson, M. Z.,Kaiser, J. W., Klimont, Z., Lohmann, U., Schwarz, J. P.,
809   Shindell,D., Storelvmo, T., Warren, S. G., and Zender, C. S.: Bounding the role of black carbon
810   in the climate system: A scientific assessment, J. Geophys. Res., 118, 1–173,
811   doi:10.1002/jgrd.50171, 2013.

812 Boucher, O., D. Randall, P. Artaxo, C. Bretherton, G. Feingold, P. Forster, V.-M. Kerminen, Y.
813   Kondo, H. Liao, U. Lohmann, P. Rasch, S.K. Satheesh, S. Sherwood, B. Stevens, and X.Y.
814   Zhang: Clouds and aerosols. In Climate Change 2013: The Physical Science Basis.
815   Contribution of Working Group I to the Fifth Assessment Report of the Intergovernmental
816   Panel on Climate Change. T.F. Stocker, D. Qin, G.-K. Plattner, M. Tignor, S.K. Allen, J.
817   Doschung, A. Nauels, Y. Xia, V. Bex, and P.M. Midgley, Eds. Cambridge University Press, pp.
818   571-657, doi:10.1017/CBO9781107415324.016, 2013.

819 Capes, G., B. Johnson, G. McFiggans, P. I. Williams, J. M. Haywood, and H. Coe, Aging of
820   biomass burning aerosols over West Africa: Aircraft measurements of chemical composition,
821   microphysical properties and emission ratios, J. Geophys. Res., 113, D00C15,
822   doi:10.1029/2008JD009845, 2008.

823 Carrico, C.M., Prenni, A.J., Kreidenweis, S.M., Levin, E.J., McCluskey, C.S., DeMott, P.J.,
824   McMeeking, G.R., Rapidly evolving ultrafine and fine mode biomass smoke physical

properties: comparing laboratory and field results, J. Geophys. Res. Atmos., 121(10), 10.1002/2015JD024389, 2016.

Chen, G., Ziemba, L. D., Chu, D. A., Thornhill, K. L., Schuster, G. L., Winstead, E. L., Diskin, G. S., Ferrare, R. A., Burton, S. P., Ismail, S., Kooi, S. A., Omar, A. H., Slusher, D. L., Kleb, M. M., Reid, J. S., Twohy, C. H., Zhang, H., and Anderson, B. E.: Observations of Saharan dust microphysical and optical properties from the Eastern Atlantic during NAMMA airborne field campaign, Atmos. Chem. Phys., 11, 723-740, https://doi.org/10.5194/acp-11-723-2011, 2011.

Chou, C., P. Formenti, M. Maille, P. Ausset, G. Helas, S. Osborne, and M. Harrison, Size distribution, shape and composition of dust aerosols collected during the AMMA SOP0 field campaign in the northeast of Niger, January 2006, J. Geophys. Res., 113, D00C10, doi:10.1029/2008JD009897, 2008.

Clarke, A., McNaughton, C., Kapustin, V., Shinozuka, Y., Howell, S., Dibb, J., Zhou, J., Anderson, B., Brekhovskikh, V., Turner, H., and Pinkerton, M.: Biomass burning and pollution aerosol over North America: organic components and their influence on spectral optical properties and humidification response, J. Geophys. Res., 112, D12S18, doi:10.1029/2006JD007777, 2007.

Corr, C. A., Hall, S. R., Ullmann, K., Anderson, B. E., Beyersdorf, A. J., Thornhill, K. L., Cubison, M. J., Jimenez, J. L., Wisthaler, A., and Dibb, J. E.: Spectral absorption of biomass burning aerosol determined from retrieved single scattering albedo during ARCTAS, Atmos. Chem. Phys., 12, 10505-10518, https://doi.org/10.5194/acp-12-10505-2012, 2012.

Deetz, K., Vogel, H., Haslett, S., Knippertz, P., Coe, H., and Vogel, B.: Aerosol liquid water content in the moist southern West African monsoon layer and its radiative impact, Atmos. Chem. Phys., 18, 14271-14295, https://doi.org/10.5194/acp-18-14271-2018, 2018.

Denjean, C., Cassola, F., Mazzino, A., Triquet, S., Chevaillier, S., Grand, N., Bourrianne, T., Momboisse, G., Sellegri, K., Schwarzenbock, A., Freney, E., Mallet, M., and Formenti, P.: Size distribution and optical properties of mineral dust aerosols transported in the western Mediterranean, Atmos. Chem. Phys., 16, 1081-1104, https://doi.org/10.5194/acp-16-1081-2016, 2016.

Deroubaix, A., Menut, L., Flamant, C., Brito, J., Denjean, C., Dreiling, V., Fink, A., Jambert, C., Kalthoff, N., Knippertz, P., Ladkin, R., Mailler, S., Maranan, M., Pacifico, F., Piguet, B., Siour, G., and Turquety, S.: Diurnal cycle of coastal anthropogenic pollutant transport over southern West Africa during the DACCIWA campaign, Atmos. Chem. Phys., 19, 473-497, https://doi.org/10.5194/acp-19-473-2019, 2019.

Di Biagio, C., Formenti, P., Doppler, L., Gaimoz, C., Grand, N., Ancellet, G., Attié, J.-L., Bucci, S., Dubuisson, P., Fierli, F., Mallet, M., and Ravetta, F.: Continental pollution in the Western

859   Mediterranean basin: large variability of the aerosol single scattering albedo and influence on
860   the direct shortwave radiative effect, Atmos. Chem. Phys., 16, 10591-10607,
861   https://doi.org/10.5194/acp-16-10591-2016, 2016.

862 Dubovik, O., Holben, B. N., Eck, T. F., Smirnov, A., Kaufman, Y. J., King, M. D., Tanre, D.,and
863   Slutsker, I.: Climatology of atmospheric aerosol absorption and optical properties in key
864   locations, J. Atmos. Sci., 59, 590–608, 2002.

865 Flamant, C., Deroubaix, A., Chazette, P., Brito, J., Gaetani, M., Knippertz, P., Fink, A. H., de
866   Coetlogon, G., Menut,L., Colomb, A., Denjean, C., Meynadier, R., Rosenberg, P., Dupuy, R.,
867   Dominutti, P., Duplissy, J., Bourrianne,T., Schwarzenboeck, A., Ramonet, M., and Totems, J.:
868   Aerosol distribution in the northern Gulf of Guinea: local anthropogenic sources, long-range
869   transport, and the role of coastal shallow circulations, Atmospheric Chemistryand Physics, 18,
870   12 363–12 389, https://doi.org/10.5194/acp-18-12363-2018, 2018a.

871 Flamant C., Knippertz, P., Fink, A. H., Akpo, A., Brooks, B., Chiu, C. J., Coe, H., Danuor, S.,
872   Evans, M., Jegede, O., Kalthoff, N., Konaré, A., Liousse, C., Lohou, F., Mari, C., Schlager, H.,
873   Schwarzenboeck, A., Adler, B., Amekudzi, L., Aryee, J., Ayoola, M., Batenburg, A. M.,
874   Bessardon, G., Borrmann, S., Brito, J., Bower, K., Burnet, F., Catoire, V., Colomb, A., Denjean,
875   C., Fosu-Amankwah, K., Hill, P. G., Lee, J., Lothon, M., Maranan, M., Marsham, J.,
876   Meynadier, R., Ngamini, J.-B., Rosenberg, P., Sauer, D., Smith, V., Stratmann, G., Taylor, J. W.,
877   Voigt, C., and Yoboué, V.: The Dynamics-Aerosol-Chemistry-Cloud Interactions in West Africa
878   field campaign: Overview and research highlights, B. Am. Meteorol. Soc., 99, 83–104,
879   https://doi.org/10.1175/BAMS-D-16-0256.1, 2018b.

880 Formenti, P., Rajot, J. L., Desboeufs, K., Saïd, F., Grand, N.,Chevaillier, S., and Schmechtig, C.:
881   Airborne observations ofmineral dust over western Africa in the summer Monsoons eason:
882   spatial and vertical variability of physico-chemicaland optical properties, Atmos. Chem. Phys.,
883   11, 6387–6410,doi:10.5194/acp-11-6387-2011, 2011.

884 Formenti, P., B. D'Anna, C. Flamant, M. Mallet, S.J. Piketh, K. Schepanski, F. Waquet, F. Auriol,
885   G. Brogniez, F. Burnet, J. Chaboureau, A. Chauvigné, P. Chazette, C. Denjean, K. Desboeufs, J.
886   Doussin, N. Elguindi, S. Feuerstein, M. Gaetani, C. Giorio, D. Klopper, M.D. Mallet, P. Nabat,
887   A. Monod, F. Solmon, A. Namwoonde, C. Chikwililwa, R. Mushi, E.J. Welton, and B. Holben,
888   0: The Aerosols, Radiation and Clouds in southern Africa (AEROCLO-sA) field campaign in
889   Namibia: overview, illustrative observations and way forward. *Bull. Amer. Meteor. Soc.,* 0,
890   https://doi.org/10.1175/BAMS-D-17-0278.1, 2019.

891 Forrister, H., Liu, J., Scheuer, E., Dibb, J., Ziemba, L., Thornhill, K. L., Anderson, B., Diskin, G.,
892   Perring, A. E., and Schwarz, J. P.: Evolution of brown carbon in wildfire plumes, Geophys.
893   Res. Lett., 42, 4623–4630, 2015.

894 Haslett, S. L., Taylor, J. W., Evans, M., Morris, E., Vogel, B., Dajuma, A., Brito, J., Batenburg, A.
895   M., Borrmann, S., Schneider, J., Schulz, C., Denjean, C., Bourrianne, T., Knippertz, P., Dupuy,
896   R., Schwarzenböck, A., Sauer, D., Flamant, C., Dorsey, J., Crawford, I., and Coe, H.: Remote
897   biomass burning dominates southern West African air pollution during the monsoon, Atmos.
898   Chem. Phys. Discuss., https://doi.org/10.5194/acp-2019-38, in review, 2019.

899 Haywood, J. M., Francis, P., Osborne, S., Glew, M., Loeb, N.,Highwood, E., Tanre, D., Myhre, G.,
900   Formenti, P., and Hirst,E.: Radiative properties and direct radiative effect of Saharan dust
901   measured by the C-130 aircraft during SHADE:1. Solar spectrum, J. Geophys. Res.-Atmos.,
902   108, 8577, https://doi.org/10.1029/2002jd002687, 2003a.

903 Haywood, J. M., S. R. Osborne, P. N. Francis, A. Keil, P. Formenti, M. O.Andreae, and P. H. Kaye,
904   The mean physical and optical properties of regional haze dominated by biomass burning
905   aerosol measured from the C-130 aircraft during SAFARI 2000, J. Geophys. Res., 108(D13),
906   8473, doi:10.1029/2002JD002226, 2003b.

907 Haywood, J. M., Pelon, J., Formenti, P., Bharmal, N., Brooks, M., et al.: Overview of the dust and
908   biomass-burning experiment and African Monsoon multidisciplinary analysis special observing
909   period-0., J. Geophys. Res., 113, doi:10.1029/2008JD010077, 2008.

910 Heintzenberg, J., The SAMUM-1 experiment over Southern Morocco: Overview and introduction,
911   Tellus Ser. B, 61, 2-11, 2009.

912 Hess, M., Koepke, P., Schult I., Optical properties of aerosols and clouds, Bull. Amer. Meteor.
913   Soc., 79, 831-844, 1998.

914 Janhäll, S., Andreae, M. O., and Pöschl, U.: Biomass burning aerosol emissions from vegetation
915   fires: particle number and mass emission factors and size distributions, Atmos. Chem. Phys.,
916   10, 1427-1439, https://doi.org/10.5194/acp-10-1427-2010, 2010.

917 Johnson, B. T., Heese, B., McFarlane, S. A., Chazette, P., Jones, A. et al.: Vertical distribution and
918   radiative effects of mineral dust and biomass burning aerosol over West Africa during DABEX,
919   J. Geophys. Res., 113(D17), D00C12, doi:10.1029/2008JD009848,2008.

920 Jolly, W. M., Cochrane, M. A., Freeborn, P. H., Holden, Z. A., Brown, T. J., Williamson, G. J., and
921   Bowman, D. M. J. S.: Climate-induced variations in global wild- fire danger from 1979 to
922   2013, Nat. Commun., 6, 7537, https://doi.org/10.1038/ncomms8537, 2015.

923 Kalthoff, N., Lohou, F., Brooks, B., Jegede, G., Adler, B., Babić, K., Dione, C., Ajao, A.,
924   Amekudzi, L. K., Aryee, J. N. A., Ayoola, M., Bessardon, G., Danuor, S. K., Handwerker, J.,

925   Kohler, M., Lothon, M., Pedruzo-Bagazgoitia, X., Smith, V., Sunmonu, L., Wieser, A., Fink, A.
926   H., and Knippertz, P.: An overview of the diurnal cycle of the atmospheric boundary layer
927   during the West African monsoon season: results from the 2016 observational campaign,
928   Atmos. Chem. Phys., 18, 2913-2928, https://doi.org/10.5194/acp-18-2913-2018, 2018.

929   Kirchstetter T. W. , Novakov, T., and Hobbs, P.: Evidence that the spectral dependence of light
930   absorption by aerosols is affected by organic carbon, J. Geophys. Res., 109,
931   D21208,doi:10.1029/2004JD004999, 2004.

932   Knippertz, P., Evans, M. J., Field, P. R., Fink, A. H., Liousse, C., and Marsham, J. H.: The possible
933   role of local air pollution in climate change in West Africa, Nat. Clim. Change, 5, 815–822,
934   https://doi.org/10.1038/nclimate2727, 2015a.

935   Knippertz, P., Coe, H., Chiu, J. C., Evans, M. J., Fink, A. H., Kalthoff, N., Liousse, C., Mari, C.,
936   Allan, R. P., Brooks, B., Danour, S., Flamant, C., Jegede, O. O., Lohou, F., and Marsham, J. H.:
937   The dacciwa project: Dynamics-Aerosol- Chemistry-Cloud Interactions in West Africa, Bulletin
938   of the American Meteorological Society, 96, 1451–1460, https://doi.org/10.1175/BAMS-D-14-
939   00108.1, http://journals.ametsoc.org/doi/10.1175/BAMS-D-14-00108.1, 2015b.

940   Knippertz, P., Fink, A. H., Deroubaix, A., Morris, E., Tocquer, F., Evans, M. J., Flamant, C.,
941   Gaetani, M., Lavaysse, C., Mari, C., Marsham, J. H., Meynadier, R., Affo-Dogo, A., Bahaga,
942   T., Brosse, F., Deetz, K., Guebsi, R., Latifou, I., Maranan, M., Rosenberg, 5 P. D., and
943   Schlueter, A.: A meteorological and chemical overview of the DACCIWA field campaign in
944   West Africa in June-July 2016, Atmospheric Chemistry and Physics, 17, 10 893–10 918,
945   https://www.atmos-chem-phys.net/17/10893/2017/, 2017.

946   Lack, D. A. and Cappa, C. D.: Impact of brown and clear carbon on light absorption enhancement,
947   single scatter albedo and absorption wavelength dependence of black carbon, Atmos. Chem.
948   Phys., 10, 4207–4220, doi:10.5194/acp-10-4207-2010, 2010.

949   Laing, J. R., Jaffe, D. A., and Hee, J. R.: Physical and optical properties of aged biomass burning
950   aerosol from wildfires in Siberia and the Western USA at the Mt. Bachelor Observatory, Atmos.
951   Chem. Phys., 16, 15185-15197, https://doi.org/10.5194/acp-16-15185-2016, 2016.

952   Lebel, T., Parker, D.J., Flamant, C., Bourles, B., Marticorena, M., Mougin, E., Peugeot, C.,
953   Diedhiou, A., Haywood, J.M., Ngamini, J.B., Polcher, J., Redelsperger, J.L., Thorncroft, C.D.:
954   The AMMA field campaigns: multiscale and multidisciplinary observations in the West African
955   region, Quarterly Journal of the Royal Meteorological Society, 136(S1), 8–33, 2010.

956   Lewis, K., Arnott, W. P., Moosmuller, H., and Wold, C. E.: Strong spectral variation of biomass
957   smoke light absorption and single scattering albedo observed with a novel dual-wavelength
958   photoacoustic instrument, J. Geophys. Res., 113, D16203, doi:10.1029/2007jd009699, 2008.

Lieke, K., Kandler, K., Scheuvens, D., Emmel, C., Von Glahn, C., Petzold, A., Weinzierl, B., Veira, A., Ebert, M., Weinbruch, S., and SchÜTz, L.: Particle chemical properties in the vertical column based on aircraft observations in the vicinity of Cape Verde Islands, Tellus B, 63, 497-511, doi: 10.1111/j.1600-0889.2011.00553.x, 2011.

Liousse, C., Assamoi, E., Criqui, P., Granier, C., and Rosset, R.: Explosive growth in African combustion emissions from 2005 to 2030, Environmental Research Letters, 9, 035003, https://doi.org/10.1088/1748-9326/9/3/035003, 2014.

Liu, D., Taylor, J. W., Crosier, J., Marsden, N., Bower, K. N., Lloyd, G., Ryder, C. L., Brooke, J. K., Cotton, R., Marenco, F., Blyth, A., Cui, Z., Estelles, V., Gallagher, M., Coe, H., and Choularton, T. W.: Aircraft and ground measurements of dust aerosols over the west African coast in summer 2015 during ICE-D and AER-D, Atmos. Chem. Phys., 18, 3817-3838, https://doi.org/10.5194/acp-18-3817-2018, 2018.

Magi, B. I., Magi A., Hobbs P.V., Schmid B., and Redemann J., Vertical profiles of light scattering, light absorption and single-scattering albedo during the dry, biomass burning season in southern Africa and comparisons of in situ and remote sensing measurements of aerosol optical depths, Journal of Geophysical Research, 108 (D13), doi:10.1029/2002JD002361, 2003.

Mallet, M., Nabat, P., Zuidema, P., Redemann, J., Sayer, A. M., Stengel, M., Schmidt, S., Cochrane, S., Burton, S., Ferrare, R., Meyer, K., Saide, P., Jethva, H., Torres, O., Wood, R., Saint Martin, D., Roehrig, R., Hsu, C., and Formenti, P.: Simulation of the transport, vertical distribution, optical properties and radiative impact of smoke aerosols with the ALADIN regional climate model during the ORACLES-2016 and LASIC experiments, Atmos. Chem. Phys., 19, 4963-4990, https://doi.org/10.5194/acp-19-4963-2019, 2019.

Mann, G. W., Carslaw, K. S., Reddington, C. L., Pringle, K. J., Schulz, M., Asmi, A., Spracklen, D. V., Ridley, D. A., Woodhouse, M. T., Lee, L. A., Zhang, K., Ghan, S. J., Easter, R. C., Liu, X., Stier, P., Lee, Y. H., Adams, P. J., Tost, H., Lelieveld, J., Bauer, S. E., Tsigaridis, K., van Noije, T. P. C., Strunk, A., Vignati, E., Bellouin, N., Dalvi, M., Johnson, C. E., Bergman, T., Kokkola, H., von Salzen, K., Yu, F., Luo, G., Petzold, A., Heintzenberg, J., Clarke, A., Ogren, J. A., Gras, J., Baltensperger, U., Kaminski, U., Jennings, S. G., O'Dowd, C. D., Harrison, R. M., Beddows, D. C. S., Kulmala, M., Viisanen, Y., Ulevicius, V., Mihalopoulos, N., Zdimal, V., Fiebig, M., Hansson, H.-C., Swietlicki, E., and Henzing, J. S.: Intercomparison and evaluation of global aerosol microphysical properties among AeroCom models of a range of complexity, Atmos. Chem. Phys., 14, 4679-4713, https://doi.org/10.5194/acp-14-4679-2014, 2014.

Mari, C. H., Cailley, G., Corre, L., Saunois, M., Attié, J. L., Thouret, V., and Stohl, A.: Tracing biomass burning plumes from the Southern Hemisphere during the AMMA 2006 wet season

993   experiment, Atmos. Chem. Phys., 8, 3951-3961, https://doi.org/10.5194/acp-8-3951-2008,

994   2008.

995 Martinorena, B. and Bergametti, G.: Two-year simulations of seasonal and interannual changes of

996   the Saharan dust emissions, Geophys. Res. Lett., 23, 1921-1924, 1996.

997 McConnell, C. L., Highwood, E. J., Coe, H., Formenti, P., Anderson, B., Osborne, S., Nava, S.,

998   Desboeufs, K., Chen, G., and Harrison, M. A. J.: Seasonal variations of the physical and optical

999   characteristics of Saharan dust: Results from the Dust Outflowand Deposition to the Ocean

1000   (DODO) experiment, J. Geophys. Res., 113, D14S05, doi:10.1029/2007JD009606, 2008.

1001 McMeeking, G. R., Fortner, E., Onasch, T. B., Taylor, J. W. Flynn, M., Coe, H., and Kreidenweis,

1002   S. M.: Impacts of non-refractory material on light absorption by aerosols emitted frombiomass

1003   burning, J. Geophys. Res.-Atmos., 119, 2014JD021750,

1004   https://doi.org/10.1002/2014JD021750, 2014.

1005 Menut, L., Flamant, C., Turquety, S., Deroubaix, A., Chazette, P., and Meynadier, R.: Impact of

1006   biomass burning on pollutant surface concentrations in megacities of the Gulf of Guinea,

1007   Atmospheric Chemistry and Physics, 18, 2687–20 2707, https://doi.org/10.5194/acp-18-2687-

1008   2018, 2018.

1009 Mertes, S., Schröder, F., Wiedensohler, A.: The particle detection efficiency curve of the TSI 3010

1010   CPC as a function of the temperature difference between saturator and condenser, Aerosol

1011   Science and Technology, 23, pp. 257-261, 1995.

1012 Mita, A., Isono, K., Effective complex refractive index of atmospheric aerosols containing

1013   absorbing substances, J. Meteorol. Soc. Jpn., 58, 69-80,

1014   https://doi.org/10.2151/jmsj1965.58.1_69 1980.

1015 Myhre, G., Samset, B. H., Schulz, M., Balkanski, Y., Bauer, S., Berntsen, T. K., Bian, H., Bellouin,

1016   N., Chin, M., Diehl, T., Easter, R. C., Feichter, J., Ghan, S. J., Hauglustaine, D., Iversen, T.,

1017   Kinne, S., Kirkevåg, A., Lamarque, J.-F., Lin, G., Liu, X., Lund, M. T., Luo, G., Ma, X., van

1018   Noije, T., Penner, J. E., Rasch, P. J., Ruiz, A., Seland, Skeie, R. B., Stier, P., Takemura, T.,

1019   Tsigaridis, K., Wang, P., Wang, Z., Xu, L., Yu, H., Yu, F., Yoon, J.-H., Zhang, K., Zhang, H.,

1020   and Zhou, C.: Radiative forcing of the direct aerosol effect from AeroCom Phase II simulations,

1021   Atmos. Chem. Phys., 13, 1853-1877, https://doi.org/10.5194/acp-13-1853-2013, 2013.

1022 Petzold, A., Rasp, K., Weinzierl, B., Esselborn, M., Hamburger, T.,Dornbrack, A., Kandler, K.,

1023   Schutz, L., Knippertz, P., Fiebig, M.,and Virkkula, A.: Saharan dust refractive index and optical

1024   properties from aircract-based observations during SAMUM 2006,Tellus B, 61 118–130, 2009

1025 Petzold, A., Veira, A., Mund, S., Esselborn, M., Kiemle, C., Weinzierl, B., Hamburger, T., Ehret,

1026   G., Lieke, K., and Kandler, K.: Mixing of mineral dust with urban pollution aerosol over Dakar

1027   (Senegal): impact on dust physico-chemical and radiative properties, Tellus B, 63, 619-634,
1028   doi: 10.1111/j.1600-0889.2011.00547.x, 2011.

1029   Pistone, K., Redemann, J., Doherty, S., Zuidema, P., Burton, S., Cairns, B., Cochrane, S., Ferrare,
1030   R., Flynn, C., Freitag, S., Howell, S., Kacenelenbogen, M., LeBlanc, S., Liu, X., Schmidt, K.
1031   S., Sedlacek III, A. J., Segal-Rosenhaimer, M., Shinozuka, Y., Stamnes, S., van Diedenhoven,
1032   B., Van Harten, G., and Xu, F.: Intercomparison of biomass burning aerosol optical properties
1033   from in-situ and remote-sensing instruments in ORACLES-2016, Atmos. Chem. Phys.
1034   Discuss., https://doi.org/10.5194/acp-2019-142, in review, 2019.

1035   Reid, J. S., Eck, T. F., Christopher, S. A., Koppmann, R., Dubovik,O., Eleuterio, D. P., Holben, B.
1036   N., Reid, E. A., and Zhang, J.: A review of biomass burning emissions part III: intensive optical
1037   properties of biomass burning particles, Atmos. Chem. Phys., 5,827–849, doi:10.5194/acp-5-
1038   827-2005, 2005.

1039   Roehrig, R., D. Bouniol, F. Guichard, F. D. Hourdin, and J. L. Redelsperger, The present and
1040   future of the west african monsoon: A process-oriented assessment of CMIP5 simulations along
1041   the AMMA transect, J. Clim., 26, 6471–6505, doi:10.1175/JCLI-D-12-00505.1, 2013.

1042   Russell M., Zhang, S.-H., Flagan, R.C., Seinfeld, J.H., Stolzenburg, M.R., Caldow, R.: Radially
1043   classified aerosol detector for aircraft-based submicron aerosol measurements, Journal of
1044   Atmospheric and Oceanic Technology, 13, 598-609, 1996.

1045   Ryder, C. L., Highwood, E. J., Rosenberg, P. D., Trembath, J., Brooke, J. K., Bart, M., Dean, A.,
1046   Crosier, J., Dorsey, J., Brindley, H., Banks, J., Marsham, J. H., McQuaid, J. B., Sodemann, H.,
1047   and Washington, R.: Optical properties of Saharan dust aerosol and contribution from the
1048   coarse mode as measured during the Fennec 2011 aircraft campaign, Atmos. Chem. Phys., 13,
1049   303–325, https://doi.org/10.5194/acp-13-303-2013, 2013.

1050   Ryder, C. L., Marenco, F., Brooke, J. K., Estelles, V., Cotton, R., Formenti, P., McQuaid, J. B.,
1051   Price, H. C., Liu, D., Ausset, P., Rosenberg, P. D., Taylor, J. W., Choularton, T., Bower, K., Coe,
1052   H., Gallagher, M., Crosier, J., Lloyd, G., Highwood, E. J., and Murray, B. J.: Coarse-mode
1053   mineral dust size distributions, composition and optical properties from AER-D aircraft
1054   measurements over the tropical eastern Atlantic, Atmos. Chem. Phys., 18, 17225-17257,
1055   https://doi.org/10.5194/acp-18-17225-2018, 2018.

1056   Sakamoto, K. M., Allan, J. D., Coe, H., Taylor, J. W., Duck, T. J., and Pierce, J. R.: Aged boreal
1057   biomass-burning aerosol size distributions from BORTAS 2011, Atmos. Chem. Phys., 15,
1058   1633–1646, doi:10.5194/acp-15-1633-2015, 2015.

1059   Sakamoto, K. M., Laing, J. R., Stevens, R. G., Jaffe, D. A., and Pierce, J. R.: The evolution of
1060   biomass-burning aerosol size distributions due to coagulation: dependence on fire and

1061   meteorological details and parameterization, Atmos. Chem. Phys., 16, 7709-7724,
1062   https://doi.org/10.5194/acp-16-7709-2016, 2016.

1063   Schladitz, A., Muller, T., Kaaden, N., Massling, A., Kandler, K.,Ebert, M., Weinbruch, S.,
1064   Deutscher, C., and Wiedensohler, A.:In situ measurements of optical properties at Tinfou
1065   (Morocco) during the Saharan Mineral Dust Experiment SAMUM 2006,Tellus B, 61, 64–78,
1066   doi:10.1111/j.1600-0889.2008.00397.x, 2009.

1067   Schuster, G. L., Dubovik, O., and Holben, B. N.:Angstrom exponent and bimodal aerosol size
1068   distributions, J. Geophys. Res., 111, D07207, doi:101029/2005JD006328, 2006.

1069   Schwarz, J. P., et al., Coatings and their enhancement of black carbon light absorption in the
1070   tropical atmosphere, *J. Geophys. Res.*, 113, D03203, doi:10.1029/2007JD009042, 2008.

1071   Seinfeld, J. H. and Pandis, S. N.: Properties of the Atmospheric Aerosol, in: Atmospheric
1072   Chemistry and Physics: From Air Pollution to Climate Change, 2nd ed., John Wiley & Sons,
1073   New Jersey, USA, 350–388, 2006.

1074   Shin, S.-K., Tesche, M., Noh, Y., and Müller, D.: Aerosol-type classification based on AERONET
1075   version 3 inversion products, Atmos. Meas. Tech., 12, 3789–3803, https://doi.org/10.5194/amt-
1076   12-3789-2019, 2019.

1077   Silva, S. and Arellano, A.: Characterizing regional-scale combustion using satellite retrievals of
1078   CO, NO2 and CO2, Remote Sensing, 9, 744, https://doi.org/10.3390/rs9070744, 2017.

1079   Solmon, F., Mallet, M., Elguindi, N., Giorgi, F., Zakey, A., and Konare, A.: Dust aerosol impact on
1080   regional precipitation over western Africa, mechanisms and sensitivity to absorption properties,
1081   Geophys. Res. Lett., 35, L24705, doi:10.1029/2008GL035900, 2008

1082   Stier, P., Schutgens, N. A. J., Bellouin, N., Bian, H., Boucher, O., Chin, M., Ghan, S., Huneeus, N.,
1083   Kinne, S., Lin, G., Ma, X., Myhre, G., Penner, J. E., Randles, C. A., Samset, B., Schulz, M.,
1084   Takemura, T., Yu, F., Yu, H., and Zhou, C.: Host model uncertainties in aerosol radiative
1085   forcing estimates: results from the AeroCom Prescribed intercomparison study, Atmos. Chem.
1086   Phys., 13, 3245-3270, https://doi.org/10.5194/acp-13-3245-2013, 2013.

1087   Stohl, A., Eckhardt, S., Forster, C., James, P., Spichtinger, N., and Seibert, P.: A replacement for
1088   simple back trajectory calculations in the interpretation of atmospheric trace substance
1089   measurements, Atmos. Environ., 36, 4635–4648, 2002.

1090   Vakkari, V., Kerminen, V. M., Beukes, J. P., Tiitta, P., van Zyl, P. G., Josipovic, M., Venter, A. D.,
1091   Jaars, K.,Worsnop, D. R., Kulmala, M., and Laakso, L.: Rapid changes in biomass burning
1092   aerosols   by   atmospheric   oxidation,   Geophys.   Res.   Lett.,   41,   2644–2651,
1093   doi:10.1002/2014gl059396, 2014.

1094   Virkkula, A., Correction of the Calibration of the 3-wavelength Particle Soot Absorption
1095   Photometer (3λ PSAP), Aerosol Science and Technology, 44:8, 706-712, DOI:
1096   10.1080/02786826.2010.482110, 2010.

1097   Wang, T., T. F. Cheung, Y. S. Li, X. M. Yu, and D. R. Blake, Emission characteristics of CO, NOx
1098   ,SO2 and indications of biomass burning observed at a rural site in eastern China, J. Geophys.
1099   Res., 107 (D12), 4157, doi:10.1029/2001JD000724, 2002.

1100   Weinzierl, B., Sauer, D., Esselborn, M., Petzold, A., Veira, A., Rose, M., Mund, S., Wirth, M.,
1101   Ansmann, A., Tesche, M., Gross, S., and Freudenthaler, V.: Microphysical and optical
1102   properties of dust and tropical biomass burning aerosol layers in the Cape Verde region—an
1103   overview of the airborne in situ and lidar measurements during SAMUM-2, Tellus B, 63, 589-
1104   618, doi: 10.1111/j.1600-0889.2011.00566.x, 2011.

1105   Wiedensohler, A., Orsini, D., Covert, D.S., Coffmann, D., Cantrell, W., Havlicek, M., Brechtel,
1106   F.J., Russell, L.M., Weber, R.J., Gras, J., Hudson, J.G., Litchy M.: Intercomparison study of
1107   size-dependent counting efficiency of 26 condensation particle counters, Aerosol Science and
1108   Technology, 27, 224-242, 1997.

1109   Yokelson, R. J., Crounse, J. D., DeCarlo, P. F., Karl, T., Urbanski, S., Atlas, E., Campos, T.,
1110   Shinozuka, Y., Kapustin, V., Clarke, A. D., Weinheimer, A., Knapp, D. J., Montzka, D. D.,
1111   Holloway, J., Weibring, P., Flocke, F., Zheng, W., Toohey, D., Wennberg, P. O., Wiedinmyer, C.,
1112   Mauldin, L., Fried, A., Richter, D., Walega, J., Jimenez, J. L., Adachi, K., Buseck, P. R., Hall,
1113   S. R., and Shetter, R.: Emissions from biomass burning in the Yucatan, Atmos. Chem. Phys., 9,
1114   5785-5812, https://doi.org/10.5194/acp-9-5785-2009, 2009.

1115   Zhong, M. and Jang, M.: Dynamic light absorption of biomass-burning organic carbon
1116   photochemically aged under natural sunlight, Atmos. Chem. Phys., 14, 1517-1525,
1117   https://doi.org/10.5194/acp-14-1517-2014, 2014.

1118   Zhai, J., Lu, X., Li, L., Zhang, Q., Zhang, C., Chen, H., Yang, X., and Chen, J.: Size-resolved
1119   chemical composition, effective density, and optical properties of biomass burning particles,
1120   Atmos. Chem. Phys., 17, 7481-7493, https://doi.org/10.5194/acp-17-7481-2017, 2017.

1121   Zuidema, P., Redeman, J., Haywood, J., Wood, R., Piketh, S., Hipondoka, M. and Formenti, P.:
1122   Smoke and clouds above the southeast Atlantic: upcoming field campaigns probe absorbing
1123   aerosols impact on climate, Bull. Am. Meteorol. Soc., doi: 10.1175/BAMS-D-15-00082.1,
1124   2016.

1125   Zuidema, P., Sedlacek III, A. J., Flynn, C., Springston, S., Delgadillo, R., Zhang, J., Aiken, A. C.,
1126   Koontz, A., Muradyan,P., and Zuidema, P.: The Ascension Island boundary layer in the remote

1127   southeast Atlantic is often smoky, Geophysical Research Letters, In Press, 4456–4465,

1128   https://doi.org/10.1002/2017GL076926, 2018.